A Preliminary Assessment of Microstructure and Mechanical Properties of 15-5 PH Stainless Steel Processed via Direct Metal Laser Sintering

A Thesis

Presented in Partial Fulfillment of the Requirements for the

Degree of Master of Science

with a

Major in Material Science and Engineering

in the

College of Graduate Studies

University of Idaho

by

Dallas Roberts

Major Professor: Indrajit Charit, Ph.D.

Committee Members: Batric Pesic, Ph.D.; Mark Roll, Ph.D.

Department Administrator: D. Eric Aston, Ph.D.

December 2019

Authorization to Submit Thesis

This thesis of Dallas Roberts, submitted for the degree of Master of Science with a major in Materials Science and Engineering and titled "A Preliminary Assessment of Microstructure and Mechanical Properties of 15-5 PH Stainless Steel Processed via Direct Metal Laser Sintering," has been reviewed in final form. Permission, as indicated by the signatures and dates given below, is now granted to submit final copies to the College of Graduate Studies for approval.

Major Professor: _____ Date: _____

Indrajit Charit, Ph.D.

Committee Members: _____ Date: _____

Batric Pesic, Ph.D.

_____ Date: _____

Mark Roll, Ph.D.

Department

Administrator: _____ Date: _____

D. Eric Aston, Ph.D.

Abstract

Additive manufacturing is a relatively new industrial technique for the manufacturing of desired shapes layer upon layer, which has, in recent years, begun to garner significant interest due to its potential, showing new possibilities in both part design and logistical trains. Because of the new way the materials are manufactured, new modeling techniques and a verification of material characteristics are required to ensure safe and economical design. Direct metal laser sintering (DMLS) is a powder bed, laser based additive manufacturing technique that already has industrial machines active and available. DMLS is popular because of its relatively high accuracy, ability to manufacture multiple parts simultaneously, and the low amount of waste produced during manufacture.

15-5 PH SS is a martensitic precipitation hardening stainless steel, used in aerospace, chemical, and other industries because of its high strength, excellent corrosion resistance, and good forgeablility. Even though this steel has been made via DMLS, there has been a lack of detailed examination of the additively manufactured material in comparison with its traditionally manufactured counterpart. In this study, tensile and creep tests performed on additively manufactured 15-5 PH showed an improvement of approximately 30% in elevated temperature tensile strength. This increase in tensile strength came at a reduction in ductility by 50%. Further, the creep life of the additively manufactured material was 30% greater when tested at 593 °C and 211 MPa. Examination of potential heat treatments of the additively manufactured alloy was also carried out, with the additively manufactured material exhibiting smaller precipitate sizes and higher Vickers microhardness.

Acknowledgements

This thesis would not have been possible without the guidance and infinite patience of Dr. Charit. He kept me going with encouragement and support though my many years here at this institution. I would also like to thank my committee members, Dr. Pesic and Dr. Roll, for their help in the process as well.

I would like to thank Dr. Tom Williams and his Graduate student Cody for their assistance with our finicky transmission electron microscope, X-ray diffraction, and scanning electron microscopes.

I would like to acknowledge Arnab Kundu, Martin Taylor, and most particularly Anumat Sittiho for their assistance in proper lab techniques and support with data collection.

I would like to thank Charles Cornwall for the assistance with prompt sample preparation.

This research was funded, in part, by the Idaho Global Entrepreneurial Mission (IGEM) grant program administered by the Idaho Department of Commerce.

Dedication

I couldn't have finished this without the support of my family, friends, and professors throughout the process. I progress on their kindness and understanding.

Thank you all.

Table of Contents

List of Figures

List of Tables

Chapter 1 Background and Literature Review

1.1 Introduction

Since mankind began shaping tools out of rocks in the distant past, all finished goods have undergone the same basic type of process, involving steady removal of material from a blank of some type, or formation of material until a final shape is achieved. These traditional processes have, in recent decades, finally been joined by several new processes which work in a fundamentally different way to attempt to achieve the same finished product.

Additive manufacturing (AM) consists of processes which, as may be deduced from the name given, reach a finished shape by the steady deposition of material [1]. This new methodology gives many exciting improvements over traditional subtractive and formative processes, such as allowing for more complex geometries in finished parts and decreased processing times required to produce finished parts [2]. But these benefits are only the beginning of the promise that can be seen in AM. Much like the train did for transportation and the printing press did for the spread of information, AM is expected to be a revolutionary technology for manufacturing.

For example, in 2010 the Navy expressed a desire to use AM techniques in the production of parts for its aircraft with multiple expected benefits [2]. A few of the specific benefits identified by the Navy were a reduction in overall energy consumption and ability to manufacture parts on demand, but these are only the beginning of the possibilities AM brings to the table [2]. Other examples of the new possibilities AM processes allow are recent advancements in the printing of organs, though still in its infancy, and the ability to manufacture flexible electronic circuits [3].

AM processes promise to revolutionize many industries but need further development and research to finish laying the groundwork necessary to utilize them in industrial quantities with full confidence in their quality. Currently, two of the largest barriers to industrial scale use of additive manufacturing are process monitors and controls, and materials qualification needs [4] [5].

One metallic alloy already in trial use in multiple additive manufacturing processes is 15-5 PH stainless steel (SS). A precipitation hardenable stainless steel, 15-5 PH is used in

industries including the aerospace, chemical, and food processing, due to several factors, including its high strength and good corrosion resistance. While the traditionally manufactured material is well understood, additively manufactured 15-5 PH requires further research to determine best practices to ensure commensurate quality [1] [4] [5].

1.1.1 Objectives

This thesis work attempts to gain understanding of the mechanical and microstructural characteristics of an additively manufactured 15-5 PH stainless steel processed via direct metal laser sintering. Mechanical integrity of these materials is not well understood. Results are discussed to lay the groundwork towards the development of post-processing heat treatments for the additively manufactured 15-5 PH Stainless Steel.

1.2 Additive Manufacturing

Though many differing names for the field have been considered, including rapid prototyping, 3D printing, and freeformed fabrication, additive manufacturing (AM) was standardized by the ASTM in January of 2009, and it was defined to be the "process of joining materials to make parts from 3D model data, usually layer upon layer, as opposed to subtractive manufacturing and formative manufacturing methodologies" [6]. While 2009 marked the beginning of standardization attempts by the ASTM, as can be inferred from the many names in use, AM had been around for a significant amount of time by then [6].

Herein the history, current state, and future of AM will be discussed, briefly overviewing AM systems capable of producing metallic products, with a focus on the process used to produce the material discussed in this thesis. Firstly, it would be helpful to describe the broad definitions under which all AM processes fall. ISO/ASTM terminology standard 52792 divides all the current AM processes into seven categories. These categories are: binder jetting, directed energy deposition, material extrusion, material jetting, powder bed fusion, sheet lamination, and vat photopolymerization [7].

Directed energy deposition is defined as an AM process "in which focused thermal energy is used to fuse materials by melting as they are being deposited. Focused thermal energy means that an energy source (e.g., laser, electron beam, or plasma arc) is focused to

melt the materials being deposited" [7]. This process is fully capable of handling metallic materials and was in fact one of the first processes to boast such a claim [8].

Sheet lamination is defined as "an AM process in which sheets of material are bonded to form an object" [7]. Also capable of manufacturing metallic products, sheet lamination could be considered one of the oldest AM processes, as similar processes have existed as early as the Blanther patent of 1892 [6]. It should be noted, however, that such processes were never considered for any application beyond their use in the specific niche for which they were developed.

Binder jetting is defined as "an AM process in which a liquid bonding agent is selectively deposited to join powder materials" [7]. This process is the source of the term 3D printing, as the first processes research stemmed from inkjet technology [6].

Powder bed fusion is defined as "an AM process in which thermal energy selectively fuses regions of a powder bed" [7]. This category includes Electro Optical Systems' (EOS) EOSINT machine which produced the material used in this thesis. Due to a variety of reasons, including their good dimensional control and ability to manufacture multiple parts simultaneously, commercial machines under the umbrella of powder bed fusion are some of the most popular metal capable AM machines on the market currently [6].

Material extrusion is defined as "an AM process in which material is selectively dispensed through a nozzle of orifice" and material jetting is defined as "an AM process in which droplets of build material are selectively deposited. Example materials include photopolymer and wax" [7]. While neither category currently boasts a commercial machine capable of taking advantage of metallic materials, nascent research into such systems has begun, and is ongoing [9] [10]. Material extrusion machines are still of particular note because, due to their low cost, they make up the majority of AM machines available to the general public, as well as due to their use in biomedical cell printing though both of these uses are outside the scope of this thesis [6].

Finally, vat polymerization is defined as "an AM process in which liquid photopolymer in a vat is selectively cured by light-activated polymerization" [7]. As may be inferred from the name, vat polymerization is incapable of manufacturing metallic products,

but must be mentioned as the first and the most popular commercial AM machines fall under this category [11] Currently, ISO/ASTM standard 52792 is under review, and is expected that an updated standard is expected to be released in the following year.

1.2.1 A Brief History of Additive Manufacturing

While most trace the beginnings of the field to the development of computer aided design (CAD) in the 1980's, processes that fall under the umbrella of AM existed as early as 1860, such as the aforementioned Blanther patent [6]. Between 1950 and the mid 1980's several technologies were invented that were limited in production ability only by the lack of CAD technology to allow for the manufacture of any arbitrary product [6].

The first processes designed with the abilities of CAD in mind began development in the early 80's, with companies built around the concept of providing AM machines forming around the same time [6] [12]. During this nascent research, the goal was to provide machines capable of allowing engineers and scientists to produce models and prototypes with rapidity and ease, leading to the emergence of the term 'Rapid Prototyping' to describe the new technique [12].

The first commercial machine to hit the market was the SLA-1, introduced in 1987 by 3D systems [13]. This first machine was quickly followed by multiple other stereolithography machines, EOS reaching the market with their own offering by 1990 [14]. The next year saw the release of several machines utilizing a process other than stereolithography. During 1992-1995, multiple nascent AM processes started to see their first commercial ventures, including EOS' first EOSINT machine [14].

In the second half of the 1990's, the prices and sizes of various AM machines began trending toward affordable, as more and more companies entered the market [14]. This trend would follow through into the 2000's, as further development of AM processes continued to bring new processes, and more capable machines to market [6] [14]. This is also when AM machines began to branch out beyond models and into places like the dental industry [14].

As the 2000's closed, the AM industry began to receive increasing interest as newer laser and electron beam based systems showed promise for fantastic applications beyond plastic models and prototypes [15]. The close of the decade saw the formation of ASTM F42

Technical Committee on Additive Manufacturing in 2009, as previously mentioned, where AM received its technical name and first technical definitions [6].

The last decade, the 2010's, has seen a rapid expansion of the AM industry, the decade beginning with military interest in the ability to produce parts on demand [15]. Since then, the AM industry has seen exponential growth, with the industry reaching $7 billion in value by 2018 [16]. Interest in the AM field continues to grow, as process controls and the understanding of the relation of process parameters to material properties improve, bringing the industry closer to its goal of mass production.

1.2.2 Directed Energy Deposition

Directed Energy Deposition (DED) is an AM technique where the process utilizes any energy source, such as a laser, to deposit flowing powder or wire in the desired shape on a substrate of some type [1]. Currently, DED processes can be divided into two separate process types. The first type is based on well understood and commonly used welding techniques, using wire as feedstock while the second type of processes use powder as a feedstock. Both types of process generally require some sort of special atmosphere, for example a protective argon atmosphere is used to prevent oxidation of the hot material under use, or a required vacuum for the function of the electron beam energy source.

An example of the first type of process is Electron Beam Freeform Fabrication (EBF) which uses a fine wire as feedstock and an electron beam as an energy source [17]. The end of the wire is melted and deposited selectively on the substrate to form the final required shape. EBF and other processes using electron beams as their energy source have excellent accuracy and provide a good surface finish on the final part with little to no post processing required, though they have a low deposition rate and require more time than other processes to manufacture parts [1].

A schematic of the Laser Engineered Net Shaping (LENS) system can be seen in Figure 1.1. As can be seen, the LENS process involves a head containing both the energy source for the process, usually a neodymium-doped yttrium aluminum garnet (Nd:YAG) laser, as well as a powder nozzle to provide feedstock inside a build chamber [1] [18]. The head focuses the laser on a point in the build where material is required, and at the same time as

feedstock powder is injected into the site. The injected powder melts, forming a small melt pool that follows the point the laser is focused on, this pool solidifies quickly as the focal point moves away, generating the part. After a layer of the required part is complete, the head moves up and away from the completed layer and begin repeating the process for the next layer.

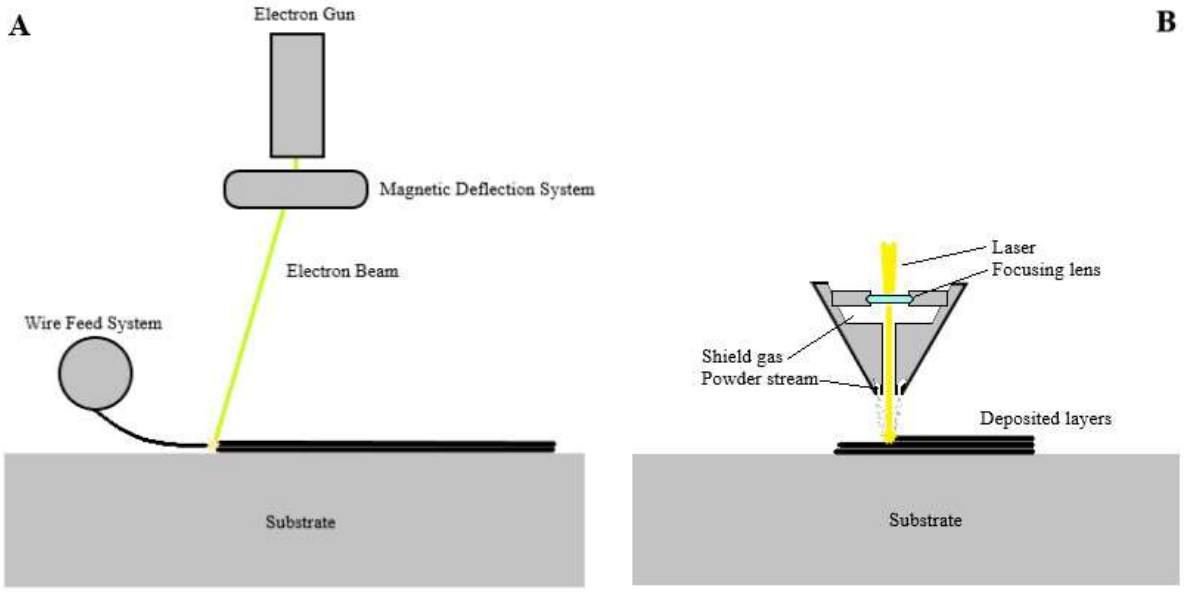

Figure 1.1: Schematic diagrams of A: EBF and B: LENS AM Systems

1.2.3 Sheet Lamination

Sheet lamination, also known as laminated object manufacturing (LOM), covers any process that uses an energy source to bond layers cut from traditionally manufactured sheets of material into the final shape [1]. Ultrasonic additive manufacturing (UAM) or ultrasonic consolidation (UC) is the most commonly used manufacturing technique [1]. A schematic of the process can be seen in Figure 1.2. Before the process, sheets of the metallic material are cut to conform with the layers required by the CAD document. The precut sheets are stacked on a base plate, and a computer controlled sonotrode moves along the rolling direction applying the required mechanical pressure and ultrasonic wave to bond the interfaces of the stacked sheets via diffusion [18]. This process is undertaken at room temperature, with the only increased temperature being due to frictional heat at the bonded interfaces of the sheets. This frictional heat necessitates a cooling period between the bonding of layers. This cooling period prevents thermal residual stresses by keeping temperatures low enough that thermal

expansion/shrinking is kept to a minimum, and insufficient heat to enable a phase change exists. At the end of manufacture, the finished part is cut from the base plate of the machine, and moves on to polishing if required, it should be noted that polishing is an option during the process as well, if required to achieve the desired finish.

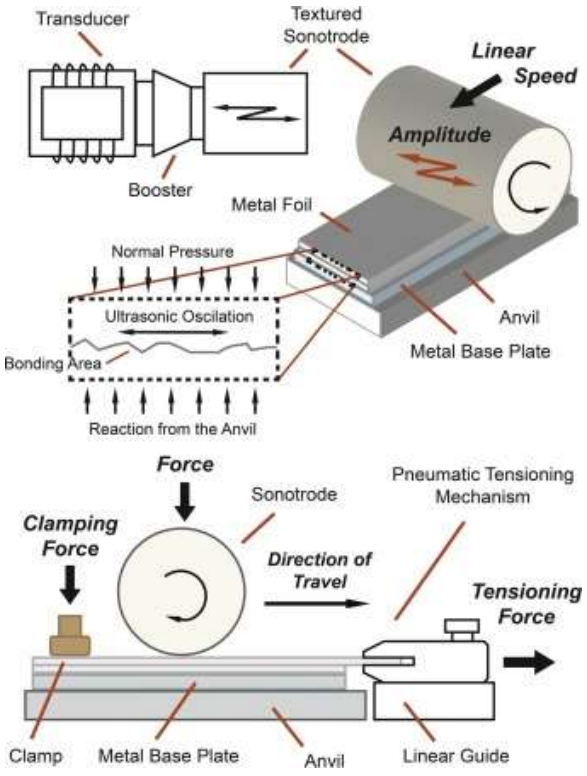

Figure 1.2: UAM Schematic [18]

1.2.4 Binder Jetting

Binder jetting is the AM process category most reminiscent of traditional printing methods, involving a powder bed and an inkjet print head [1] [19]. The overall practice of binder jetting machines involves the use of a number of nozzles to inject some type of binder material on a bed of powder, to glue the powder together [19]. Figure 1.3 shows a schematic of a typical binder jetting system. The first step in the process is to evenly distribute a layer of powder on the build envelope, usually by use of a roller or rake of some type. The print head then lowers into position, distributing binder to the powder in the areas outlined in the CAD file. After the layer has been completed, the build platform lowers, and another layer of powder is distributed. This process repeats itself until the desired shape has been attained, producing a green body that is then sent on for post-processing [19].

Post-processing of binder jetted objects has a much greater importance and complexity than what is required by objects produced via other AM techniques, especially when metallic materials are the powder medium of choice [19]. A green body made of a metallic material will first require a curing step, from anywhere between 6 to 12 hours [19]. After the curing step, the green body then undergoes a heat treatment step of 24-36 hours above 1000°C to induce consolidation and sintering of the green body [19]. Further processing than this is a consideration, such as allowing infiltration of a secondary metal to improve ductility [19].

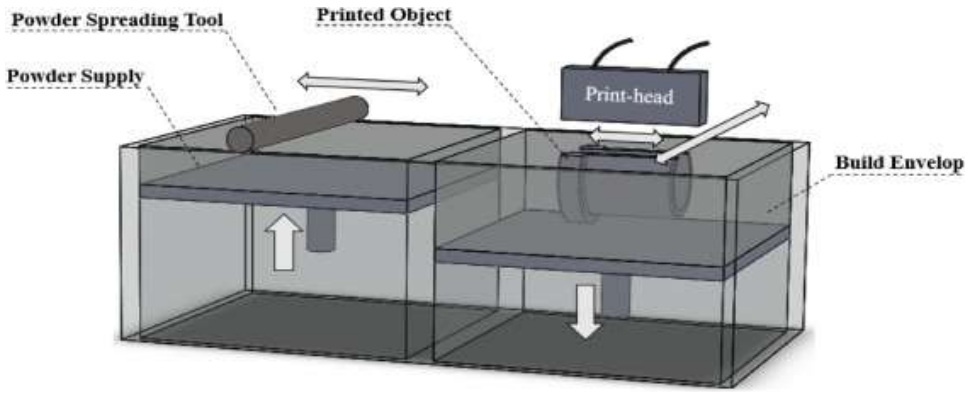

Figure 1.3: Schematic of a binder jetting machine. [20]

1.2.5 Powder Bed Fusion

The Powder Bed Fusion (PBF) category of AM processes contains under its umbrella any process where the feedstock is fused in a bed via an energy source [1] [7]. All PBF processes can then be further subdivided into two categories based on the energy source used in said process. These categories are Selective Laser Melting (SLM), and Electron Beam Melting (EBM) [1].

EBM processes utilize an electron beam in a vacuum atmosphere to fuse their feedstock, while SLM type processes make use of a laser in an inert atmosphere of either argon or nitrogen, depending on the feedstock material [1] [15]. Other than the difference of energy source and required atmosphere, the procedure involved is nearly identical, so herein focus will be placed on the direct metal laser sintering (DMLS) process. As this process is of primary focus, the particulars of the process will be covered herein.

The DMLS process begins with a metal powder that already has the required composition, according to S. Sarkar et al. [21]. EOS manufactures their feedstock powders via a gas atomization process. In a gas atomization process, liquid alloy is dispersed in a collection chamber via rapid expansion of gas out of a nozzle that both high pressure inert gas and the alloy melt are introduced into. The melt is disintegrated into small liquid particles that cool in a collection chamber from which the particles can be collected and filtered to the appropriate sizes. In the case of DMLS feedstock powder, reported particle sizes are from 5-60 μm [21] [22]. The choice of inert gas during the atomization phase of the operation is one of the first that can have an impact on the final product. For example, nitrogen is a common inert gas used in many applications that require an inert atmosphere, but in iron-based alloys it is also an austenite phase stabilizer [23] [24]. It has been shown that 15-5 PH powder gas atomized in a nitrogen environment demonstrated a higher nitrogen content than would be expected in conventional bar stock 15-5 PH, which could require alteration to its heat treatment schedule [23].

A schematic of a DMLS machine can be seen in Figure 1.4. The feedstock powder is loaded into the DMLS machine, and an inert gas is pumped in. The choice of inert atmosphere can have a large effect on the final microstructure of the finished part. As an example, due to nitrogen's higher thermal conductivity compared to argon, SLM 17-4 PH stainless steel will have a different crystal structure depending on the atmosphere [24]. Therefore, the choice of

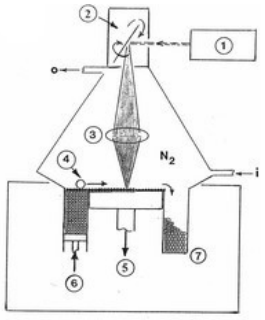

Figure 1.4: Schematic of a DMLS machine. 1. Laser source; 2. Beam deflection/scanning mirror; 3. Beam focus; 4. Powder layer roller; 5. Build table; 6. Powder Supply; 7. Excess powder. Ref. [25]

inert atmosphere is critical, as thermal conductivity, and thus the rate of cooling the part undergoes, has quite a great effect on the microstructures of produced parts, and can even be seen when comparing the length of an individual part [24].

Once an inert atmosphere is established, a rake, or roller is used to spread the powder in a layer over the build platform. In order to achieve repeatable results, with a minimal inhomogeneities, an even layer of powder with a flat surface is required to ensure good energy absorption [24]. This limits the size of the powder bed, and hence the size of the parts that can be manufactured, due to the limits of the mechanisms creating these layers [24]. Powder layer thickness can be anywhere from 20 to 100 μm [21] [24].

After a layer of powder has been spread over the build platform, the laser is powered, and the beam deflection mirror scans it across the powder layer. While the area that is sintered is determined by the CAD file, there are several parameters related to the laser itself that are controlled by the AM machine. These parameters are; the laser wattage; the spot diameter; the scanning speed; the hatch distance; and the scanning pattern. Laser wattage is the power of the laser, as may be assumed. Laser wattage in DMLS machines varies and can be anywhere from 200W and up. The spot diameter is determined by the beam focus and is the size of the area the laser power is spread across. Scanning speed determines how much time the laser spends on any one place in the pattern and is usually anywhere from 800 to 1200 mm/s [26]. Hatch distance is a measure of the distance between the center of the lasers spot as it passes across the powder. The scanning pattern is the pattern used in traversing across the bed. As may be assumed, there are multiple differing patterns that can be used to cover the powder bed. A zig zag pattern or parallel lines are common, and it is also common for the pattern to be rotated anywhere from 45 to 90° every layer to ensure full sintering of the powder [22] [24] [26]. Upon completion of a layer, the build table lowers down the thickness of an additional layer, and the process repeats, until all layers have been sintered together.

After the final part has been allowed to cool, it is removed, and the unsintered powder is reclaimed. This is done by first collecting the powder from the build platform by brush, then using an 80 μm opening sieve to remove the particles that are too large to be suitable for further use [27]. The reclaimed powder is then returned to the powder supply of the machine. This powder has been characterized in some instances, and shows no significant difference

from new powder, but concerns over powder oxidation and impurities that may make their way into recycled powder via either the atmosphere or some other method is still a concern under investigation [24] [27].

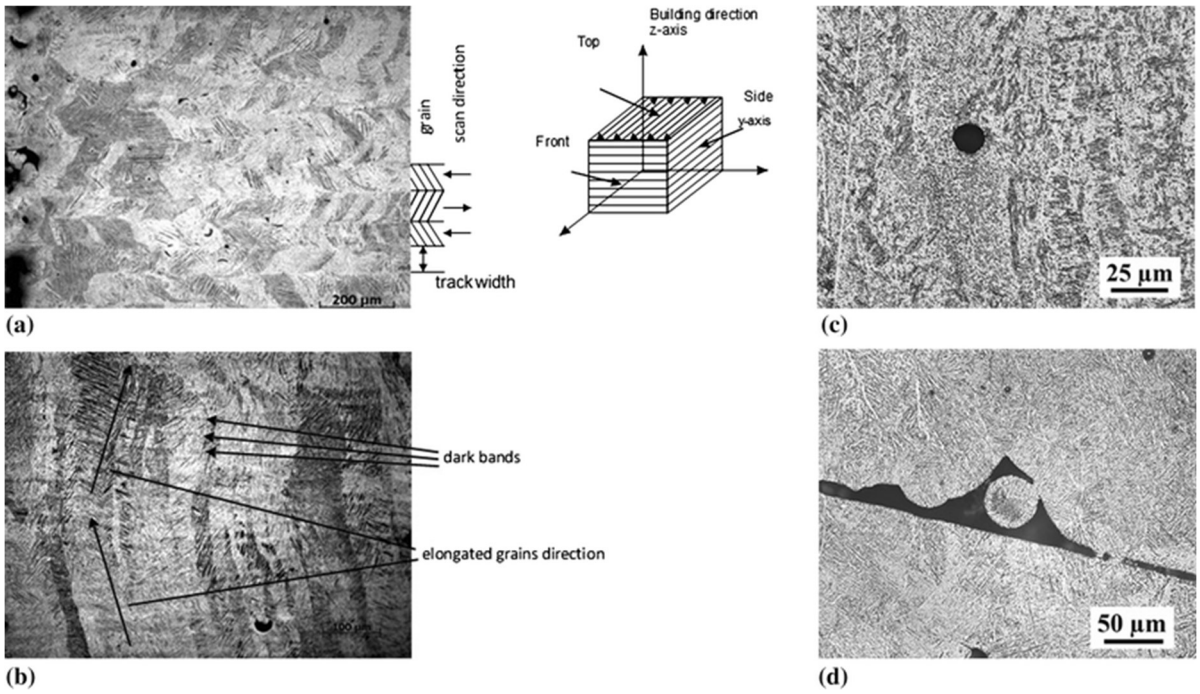

Figure 1.5: Microstructure of SLM manufactured Ti-6AL-4V (a) Top View, (b) Side View, (c) Pore due to trapped gas, (d) pore due to insufficient heating. [28]

The DMLS manufacturing process has a distinct effect on the microstructures exhibited by the final parts, and from there an effect on the properties of the material thus produced. The final microstructure of the part is very reliant on two factors: the temperature gradient and the solidification interface velocity [1] [24]. These two factors can be controlled by process parameters such as scan speed and energy source power [1] [24] [25]. Process parameters need to be fine-tuned for each material to achieve a desired microstructure. Figure 1.5 shows the microstructure that most powder bed processes generally produce. In figure 1.5(a), parallel grains with a band shaped patterns can easily be seen, growing in a hatch pattern associated with the direction of the laser as the material was being fused. Figure 1.5(b) shows how the grains grow vertically, previously fused material acting as a nucleation site. Figure 1.5(c) and (d) show potential defects associated with PBF processes, (c) shows a void caused by captured gas, whereas (d) shows a point with insufficient heating to fuse the powder.

While captured gas can happen anywhere in the material, generally defects due to insufficient heating will only occur on the edges of the fused material [1].

1.3 15-5 PH Stainless Steel

15-5 PH stainless steel is a martensitic precipitation hardening stainless steel, also known as XM-12 or UNS S15500 [29] [30]. Precipitation hardening SS were developed to deliver higher strength than was possible in austenitic and ferritic SS, and better ductility and toughness than non-precipitation hardening martensitic SS [31]. 15-5 PH SS was modified from 17-4 PH SS in the 1960's to have a more refined microstructure, and therefore better toughness [29]. 15-5 PH SS also has good fabrication properties and excellent corrosion resistance, making it a good choice for parts like gas turbine compressor sections, gears, and nuclear reactor components [29].

Precipitation hardening stainless steels achieve strengthening via the precipitation of small second phase particles in either an austenitic or a ductile low-carbon martensitic matrix [31]. The matrix material, whether austenite or martensite, is dictated by the balance of alloying elements in the alloy [31]. Precipitation hardening SS can be divided into three types, either martensitic, semi-austenitic, or austenitic, determined by what phase of iron is present in the matrix of the material [31]. All three of these types of SS undergo aging treatments at relatively low temperatures, with 500-700 °C temperatures being common, but higher and lower temperatures are also possible [31]. Martensitic precipitation hardening stainless steels, like 15-5 PH, are characterized by low carbon and nickel, and stabilizing additions that minimize carbon in solution [31]. The goal of this chemistry is to lower the austenite stability, causing it to transform to low-carbon martensite at room temperatures [31].

1.3.1 Chemistry of 15-5 PH

The chemical composition of 15-5 PH SS is listed in Table 1.1. As has been discussed, these elements each have their own effect on the microstructure and mechanical properties of the alloy.

Chromium: Arguably the most important of the alloying elements as it pertains to stainless steels, chromium increases the steels resistance to corrosion and oxidation due to the formation of a passive layer on the surface of the steel [30] [32]. Stainless steels must, by definition, have greater than a 10.5 wt% chromium content [32].

Table 1.1: Chemical Composition of 15-5 PH Stainless Steel

Element	Content (wt.%)
Iron, Fe	75
Chromium, Cr	14.48
Nickel, Ni	4.5
Copper, Cu	3.5
Manganese, Mn	≤1
Silicon, Si	≤1
Nb + Ta	0.3
Carbon, C	≤0.07
Phosphorous, P	≤0.04
Sulfur, S	≤0.03

Nickel: In stainless steels, nickel content assists in improving corrosion and oxidation resistance, as well as improving the steel toughness and fatigue resistance [30] [32].

Copper: When present in concentrations above 0.2 wt%, copper improves the resistance of the steel to salt water and acidic environments and can also produce a precipitation hardening effect [30] [32].

Manganese: Added for its beneficial effect on strength, toughness, and hardenability, manganese also improves hot working properties [30] [32]. Manganese also helps to retard the formation of iron sulfides that can reduce the high temperature strength of the steel [30].

Silicon: One of the principal deoxidizers in the steelmaking process, silicon can also increase the strength and hardness of a steel in the as-rolled condition [30] [32].

Carbon: The principle hardening element of steel, carbon increases the hardness and strength of the steel at the cost of ductility and weldability with increasing amounts [30] [32]. Additionally, carbon forms ‘carbide’ precipitates with other alloying elements, which can be either beneficial or detrimental to the properties of the steel [30].

Phosphorus and sulfur: In small amounts, these alloying elements can improve the machineability of the steel [30] [32]. Unfortunately, they also have detrimental effects on the corrosion resistance and weldability of the steel [30] [32].

Though not present on the list of alloying elements, nitrogen has a great effect on the phase present in the steel. Nitrogen acts as an austenite stabilizer, which reduces the martensite start and finish temperatures, and can prevent full transformation to martensite in the steel [23].

1.3.2 Microstructure and the Effect of Aging in 15-5 PH

As has been covered, the matrix material of the 15-5 PH microstructure is martensite. Martensite is a metastable phase of iron that forms when austenite is cooled faster than carbon can diffuse in the microstructure, causing a shear transformation of the austenite [33]. This shear transformation shifts the iron to a BCT or BCC crystal structure, depending on carbon concentration, with carbon trapped in one or more of the octahedral sites [33]. In addition to the crystal structure difference, martensite can have multiple differing morphologies depending on carbon concentration as well [33].

15-5 PH is a low carbon martensite, which means in its unaged state it forms into a BCC structure with a lath morphology and a high dislocation density [33] [34] [35]. At this point there are several other constituents contained in the microstructure. Retained austenite is one of these constituents, usually in small amounts around 0.2% [35]. The other constituents in the microstructure at this point are Niobium carbides, and Chromium carbides fairly dispersed through the matrix [34] [35].

At this point in time, the main strengthening mechanisms are the strengthening mechanisms of martensite, the main two of which are grain size strengthening and dislocation strengthening [33]. Grain size strengthening in martensite has been shown to follow the Hall-Petch relationship with effective grain size [33]. Dislocation strengthening in lath martensite is known to follow a Taylor hardening model [33].

As a precipitation hardening stainless steel, the effect of aging on the microstructure of 15-5 PH is mainly precipitation [34] [35]. In 15-5 PH, nanoscale coherent copper particles begin to precipitate homogeneously within the microstructure [35]. These precipitates are the main strengthening mechanism of the alloy, via the effect of particle shearing.

Aging has several other effects on the microstructure of 15-5 PH. The first of these is the formation of further carbides, of the $M_{23}C_6$ type [34]. These additional carbides remove

alloying elements from the microstructure on a local level, resulting in the reversion of some martensite to austenite [34]. Typically, the volume fraction of austenite in the microstructure increases to around 1-2% during aging [35].

References

[1] Y. Zhang, L. Wu, X. Guo, S. Kane, Y. Deng, Y. Jung, J. Lee, J. Zhang, "Additive Manufacturing of Metallic Materials: A Review," Journal of Mat. Eng. and perf., vol. 27, no. 1, pp. 1-13, 2018.

[2] W. Frazier, "Metal Additive Manufacturing: A Review," Journal of Mat. Eng. And Perf., Vol 23, no. 6, pp. 1917-1928, 2014.

[3] L. Murr, "Frontiers of 3D Printing/Additive Manufacturing: from Human Organs to Aircraft Fabrication," Journal of Mat. Sci. & Tech., Vol. 32, no. 10, pp. 987-995, 2016.

[4] M. Seifi, A. Salem, J. Beuth, O. Harrysson, J. J. Lewandowski, "Overview of Materials Qualification Needs for Metal Additive Manufacturing," JOM, Vol. 68, no. 3, pp. 747-764, 2016.

[5] G. Tapia, A. Elwany, "A Review on Process Monitoring and Control in Metal-Based Additive Manufacturing," Journal of Manuf. Sci. and Eng., vol. 136, no. 6, 2014.

[6] D. Bourell, "Perspectives on Additive Manufacturing," Annu. Rev. Mater. Res., vol. 46, pp. 1-18, 2016.

[7] ASTM, "Standard Terminology for additive manufacturing – general principles. Part 1: Terminology," ISO/ASTM stand. 52792, 2015.

[8] W. J. Sames, F. A. List, S. Pannala, R. R. Dehoff, S. S. Babu, "The Metallurgy and Processing Science of Metal Additive Manufacturing," International Mat. Reviews, Vol 61, no. 5, pp. 315-360, 2016.

[9] C. Ladd, J. So, J. Muth, M. D. Dickey, "3D Printing of Free Standing Liquid Metal Microstructures," Avanced Mat., vol. 25, no 36, pp. 5081-5085, 2013.

[10] C. W. Visser et al, "Toward 3D Printing of Pure Metals by Laser-Induced Forward Transfer," Advanced Mat., vol. 27, no. 27, pp 4087-4092, 2015.

[11] K. Wong, A. Hernandez, "A Review of Additive Manufacturing," ISRN Mech. Eng., vol. 2012, 2012.

[12] W. J. Sames, F. A. List, S. Pannala, R. R. Dehoff, S. S. Babu, "The Metallurgy and Processing Science of Metal Additive Manufacturing," Int. Mat. Rev., Vol. 61, no. 5, pp 315-360, 2016.

[13] B. O'Neal, *Celebrating Chuck Hull & the SLA-1 Original 3D Printer – Now a Historic Mechanical Engineering Landmark*, May 19, 2016. Accessed on: Aug. 20, 2019. [Online]. Available: https://3dprint.com/134861/chuck-hull-asme-landmark/

[14] T. Wohlers, T. Gornet, "History of Additive Manufacturing," in *Wohlers Report 2014,* Fort Collins, CO: Wohlers Associates, 2014, sec. 1, pp. 14-17. Accessed on: Aug. 21, 2019. [Online]. Available: http://wohlersassociates.com/history2014.pdf

[15] W. Frazier, "Metal Fabrication by Additive Manufacturing Using Laser and Electron Beam Melting Technologies," J. Mater. Sci. Technol., Vol. 28, no. 1, pp. 1-14, 2012.

[16] T. J. McCue, "Wohlers Report 2018: 3D Printer Industry Tops $7 Billion," Forbes, Jun 4, 2018. Accessed on: Aug. 23, 2019. [Online]. Available: https://www.forbes.com/sites/tjmccue/2018/06/04/wohlers-report-2018-3d-printer-industry-rises-21-percent-to-over-7-billion/#4bf9f35a2d1a

[17] K. M. B. Taminger, R. Hafley, "Electron Beam Freeform Fabrication: A Rapid Metal Deposition Process," in *Proceedings of the 3rd Annual Automotive Composites Conference,* Troy, MI, 2003, Accessed on: Sept. 20, 2019. [Online]. Available: https://ntrs.nasa.gov/archive/nasa/casi.ntrs.nasa.gov/20040042496.pdf

[18] A. Bournias-Varotsis, R. Friel, R. Harris, D. Engstrøm, "Ultrasonic Additive Manufacturing as a form-then-bond process for embedding electronic circuitry into a metal matrix," Journal of Manufacturing Processes, Vol. 32, pp. 664-675, 2018. Doi: https://doi.org/10.1016/j.jmapro.2018.03.027

Figure 1.2 used under Creative Commons License

[19] M. Ziaee, N. Crane, "Binder Jetting: A review of process, materials, and methods," Additive Manufacturing, Vol. 28, pp 781-801, 2019.

[20] Reprinted from Additive Manufacturing, Vol. 28, Mohsen Ziaee & Nathan Crane, Binder Jetting: A review of process, materials, and methods, Pages No. 781-801, Copyright 2019, with permission from Elsevier.

[21] S. Sarkar, C. S. Kumar, A. K. Nath, "Effects of heat treatment and build orientations on the fatigue life of selective laser melted 15-5PH stainless steel," Materials Science and Engineering: A, Vol. 755, pp 235-245, 2019.

[22] T. Hsu, Y. Chang, C. Huang, H. Yen, C. Chen, K. Jen, A. Yeh, "Microstructure and property of a selective laser melting process induced oxide dispersion strengthened 17-4 PH stainless steel," Journal of Alloys and Compounds, Vol. 803, pp 30-41, 2019.

[23] K. Coffy, "Microstructure and Chemistry Evaluation of Direct Metal Laser Sintered 15-5 PH Stainless Steel," M. S. Thesis, Dept. of Mat. Sci. & Eng., Uni. of Central FL, Orlando, FL, 2012. Accessed on Sept. 20, 2019. [Online] Available: http://etd.fcla.edu/CF/CFE0005317/Coffy_Kevin_M_MS_Final.pdf

[24] L. E. Murr, "A Metallographic Review of 3D Printing/Additive Manufacturing of Metal and Alloy Products and Components," Metallography, Microstructure, and Analysis, Vol 7, No. 2, pp 103-132, 2018.

[25] Reprinted from Journal of Material Science & Technology, Vol. 28, no. 1, L. E. Murr et al, pp. 1-14, 2012, with permission from Elsevier

[26] L. E. Murr, E. Martinez, K. Amato, S. Gaytan, J. Hernandez, D. Ramirez, P. Shindo, F. Medina, R. Wicker, "Metal Fabrication by Additive Manufacturing Using Laser and Electron Beam Melting Technologies," Journal of Materials Science & Technology, Vol. 28, no. 1, pp. 1-14, 2012.

[27] J. A. Slotwinski, E. J. Garboczi, P. E. Stutzman, C. F. Ferarris, S. S. Watson, M. A. Peltz, "Characterization of Metal Powders Used for Additive Manufacturing," J. Res. Natl. Inst. Stand. Technol., Vol. 119, pp. 460-493, 2014.

[28] Reprinted by permission from Springer Nature Customer Service Centre GmbH: Journal of Materials Engineering and Performance, 'Additive Manufacturing of Metallic Materials: A Review,' Y. Zhang, X Guo, Y. Deng Y. Jung, J. Lee, J. Zhang, © ASM

International 2017, (April 2017). Reprinted from Engineering Failure Analysis, vol. 69, "Microstructure, static properties, and fatigue crack growth mechanisms in Ti-6Al-4V fabricated by additive manufacturing: LENS and EBM," pp. 3-14, Copyright 2016, with permission from Elsevier. Reprinted from Acta Materialia, vol. 59, issue 9, "A study of the microstructural evolution during selective laser melting of Ti–6Al–4V," pp. 3303-3312, Copyright 2010, with permission from Elsevier.

[29] AZoM, "Stainless Steel Grade 15-5 PH (UNS S15500)." AZO Materials. https://www.azom.com/article.aspx?ArticleID=9134#:~:targetText=Stainless%20steel%2015%20%E2%80%93%205%20PH,improves%20toughness%20of%20the%20material. (accessed Nov. 19, 2019)

[30] *Metals Handbook, Volume 1: Properties and Selection: Irons, Steels, and High-Performance Alloys,* 10th ed., ASM International, Materials Park, OH, USA, 1990.

[31] G. Krauss, *Steels: Processing, Structure, and Performance.* Materials Park, OH, United States: ASM International, 2005.

[32] *Alloying Elements in Stainless Steel,* AALCO Metals Ltd., 18 July 2019. [Online]. Available: http://www.aalco.co.uk/datasheets/Stainless-Steel_Alloying-Elements-in-Stainless-Steel_98.ashx

[33] S. C. Kennett, "Strengthening and Toughening Mechanisms in Low-C Microalloyed Martensitic Steel as Influenced by Austenite Conditioning," Ph.D. dissertation, Dept. of Metall. and Mater. Eng., CO School of Mines, Golden, CO, U.S., 2014. [Online]. Available: https://mountainscholar.org/bitstream/handle/11124/439/Kennett_mines_0052E_10444.pdf?sequence=1&isAllowed=y

[34] H.R. Bajguirani, "The effect of ageing upon the microstructure and mechanical properties of type 15-5 stainless steel," Mat. Sci. & Eng. A, Vol. 338, No. 1-2, pp. 142-159, 2002.

[35] L. Couturier, F. De Geuser, M. Descoins, A. Deschamps, "Evolution of the microstructure of a 15-5PH martensitic stainless steel during precipitation hardening heat treatment," Mat. & Des., Vol. 107, pp. 416-4 25, 2016.

Chapter 2 A Comparative Study of Microstructure and High Temperature Mechanical Properties of 15-5 PH Stainless Steel Processed via Additive Manufacturing and Traditional Manufacturing

Reprinted by permission from Springer Nature Customer Service Centre GmbH: Springer Nature Progress in Additive Manufacturing "A Comparative Study of Microstructure and High Temperature Mechanical Properties of 15-5 PH Stainless Steel Processed via Additive Manufacturing and Traditional Manufacturing" D. Roberts, Y. Zhang, I. Charit et al, 2018

Abstract

In the present study, 15-5 PH Stainless Steel (SS) was produced via an additive manufacturing (AM) technique known as Direct Metal Laser Sintering (DMLS). The microstructure and mechanical properties of the AM alloy were compared with those of a traditionally manufactured (TM) or wrought 15-5 PH SS. Microstructural examination of both materials is performed by optical microscopy, transmission electron microscopy and electron backscatter diffraction in a scanning electron microscope. A distinct difference was observed between the martensitic structure of the AM and TM alloy with the AM material with smaller grain sizes and round-shaped particles. The Vickers microhardness of the AM material was found to be greater than that of the TM material. Tensile testing at 593 ºC exhibited a greater strength for the AM material compared to the TM material. Furthermore, the creep rupture life of the AM material was found to be greater compared to the TM material when tested at a temperature 593 ºC and applied stress of 211 MPa. Fractographic examination of the crept and tensile specimens was conducted via scanning electron microscopy.

Keywords: *Additive Manufacturing; Direct Metal Laser Sintering; 15-5 PH Stainless Steel; Creep; Tensile Testing; Microhardness*

2.1 Introduction

Additive manufacturing (AM) is a relatively new, rapidly growing field with great potential to shape nearly all levels of manufacturing. AM has been broadly defined to cover any method of manufacturing parts from 3D model data, building products layer upon layer, rather than removing material to shape a blank to required specifications (i.e. subtractive

manufacturing) [1] [2]. From its roots in polymer-based rapid prototyping developed in the late 80's and early 90's, to recent use in the production of complicated metal parts unable to be manufactured traditionally, AM promises to change global logistics, increase manufacturing energy efficiency, and reduce environmental impact [1] [2]. Although AM shows such promise, there are several hurdles to surmount before true large scale, versatile industrial applications of the technique becomes successful. One of the primary issues is the lack of an AM materials property database [1]. The investigation of materials for use in AM machines, and the development of said database of alloys have mostly focused on Ti-6Al-4V even though recently more metallic alloys have been investigated [1]. One such alloy class is the precipitation hardnenable stainless steels (SS) with the majority of the research work being focused on 17-4 PH SS [3]-[6]. However, a variant of 17-4 PH SS, 15-5 PH SS, is the material studied in this work. The material is used in multiple industries, including the aerospace, chemical, and food processing industries owing to its good combination of high strength, good corrosion resistance, good transverse toughness and good forgeability [2]. However, studies on AM 15-5 PH SS have been quite limited [7]-[9].

Multiple AM techniques have been developed over the last couple of decades, and one of those techniques, Direct Metal Laser Sintering (DMLS), has been applied to 15-5 PH SS in the present study. DMLS is another name coined for Selective Laser Sintering (SLS) to differentiate processes involving metal powders from those involving polymer powders, due to differing laser wavelengths used [10] [11]. The majority of DMLS machines are fed via powder bed, with a work area that is covered with powder via a rake, which is then sintered by the heat created by the laser into the desired geometry under an inert atmosphere [1]. In fact, it is a special category under the laser powder bed fusion (PBF) process and involves partial melting. Advantages of this system include a high resolution for features, an ability to create internal passages, and good dimensional control [1]. However, care must be taken to ensure the parameters of the laser are well adjusted to deliver the appropriate energy density to the feed powder. If the energy density is too low, incomplete sintering of the powder layer will occur, whereas too high an energy density could cause inhomogeneities via uneven melting, or vaporization of materials if the powder decomposition energy is reached [10] [11].

Interestingly only a few studies on DMLS manufactured steel of this type are found in the open literature [7]-[9]. Moreover, to the best of authors' knowledge high temperature

mechanical property data of these AM materials are not available, which are critically needed for high temperature application of the material. The current study constitutes a preliminary investigation on microstructural characteristics, microhardness and high temperature mechanical property data of this AM 15-5 PH SS in comparison to the traditionally manufactured (TM) or wrought material. The mechanical data are also supplemented with microstructural and fractographic results.

2.2 Experimental

The AM samples were prepared by an EOSINT M270 (EOS GmbH Electro Optical Systems, Germany) machine equipped with a 200 W single mode Yb fiber laser with a wavelength of 1070 nm. Processing parameters were as following: laser power of 170 W, a scanning speed of 1250 mm/s in continuous wavelength mode, a spot size of approximately 50 μm, hatch spacing of 100 μm, and a layer thickness of 30 μm. Processing was carried out under an argon environment to prevent oxidation.

The feed powder used was EOS Stainless Steel PH1, a 15-5 PH powder that conforms to standard 15-5 PH chemistry, nominal composition of which is Fe (balance), Cr (14 – 15.5 wt%), Ni (3.5 – 5.5 wt%), Cu (2.5 – 4.5 wt%), Mn (max. 1 wt%), Si (max. 1 wt%), Mo (max. 0.5 wt%), Nb (0.15 - 0.45 wt%), and C (max. 0.07 wt%). The AM samples were printed into cylindrical rods with 15 mm diameter × 90 mm length for later sectioning. Following DMLS, only a low-temperature stress-relieving heat treatment was applied to the printed parts, which was not enough to alter microstructure or mechanical properties. TM (i.e. wrought) 15-5 PH SS round bars were procured from the marketplace as cylindrical bar stock of 25 mm diameter. Unfortunately, the exact processing conditions are not known.

Room temperature density measurement of both samples was performed following the Archimedean principle. This was done to ensure that the density of the TM and AM materials are comparable. Density of both the materials were found to be about 7.8 g/cm^3.

Both tensile and creep specimens were machined from the above-mentioned cylindrical rods/bars of TM and AM materials along the longitudinal direction. Both creep and tensile specimens were kept cylindrical, and the gauge length and gauge diameter were 25.4 mm and 6.4 mm, respectively. Creep tests on both TM and AM specimens were carried out in an ATS Series 2320 MM Lever Arm Creep Tester at 593°C and 211 MPa. Tensile tests

were carried out using an Instron 5982 testing system at 593°C with a strain rate of 10^{-3} s^{-1}. One AM specimen was tested at room temperature at a strain rate of 10^{-3} s^{-1}. Due to a lack of enough samples, only one sample of each type was available for these tests.

Samples for microhardness and TEM were sectioned using via diamond wafering blade, and hot mounted in black phenolic mounting powder with a Pace Technologies Mounting Press at 170 °C. These samples were then ground from 250 to 1200 grit and polished to a final surface finish of 0.1 μm. Metallographic samples were etched with Aqua Regia (3 part hydrochloric acid and 1 part nitric acid, by volume).

Vickers microhardness tests were carried out on the samples, one from each cross-section (transverse and longitudinal) of the TM and AM materials, using a Leco LM100 Microhardness Tester with a load of 0.5 kg_f with a standard dwell time of 15 s. For each sample face, 17 indentations were made.

Metal sections from both AM and TM materials were thinned below 100 μm, punched into 3-mm diameter disks, and jet polished using an electrolyte of composition 15 vol% nitric acid and 85 vol% methanol in a Fischione twin-jet electropolisher at about -35 ^{o}C. They are examined using a JEOL 2010J TEM at an accelerating voltage of 200 kV.

Scanning electron microscopy was performed to examine the fracture surfaces of the AM creep and tensile samples under secondary electron imaging mode in a Zeiss Supra 35 Scanning Electron Microscope (SEM) at an accelerating voltage of 10 kV. Electron backscatter diffraction (EBSD) studies were undertaken in the same SEM using a Quasor Electron Backscatter Diffraction system controlled by Fisher ThermoScientific NSS software. An accelerating voltage of 20 kV on the high current setting was used to capture the data, and a pixel binning of 4×4 was used to minimize noise and information loss. Samples for EBSD were prepared in the same way as the TEM samples, with less time spent to prevent the formation of a hole during electro-jetpolishing. The preparation method was adequate for creating the damage-free surface condition for EBSD studies.

2.3. Results and Discussion

2.3.1. Microstructural Examination

The microstructural characterization was performed using optical microscopy. Figure 2.1(a) shows an optical micrograph of the TM 15-5 PH SS in the transverse cross-section. On

the other hand, Figure 2.1(b) shows an optical micrograph taken from the longitudinal cross-section. The microstructures in two perpendicular sections appear quite similar and mainly consist of martensitic structure. It is worth noting that examination of the as-polished surfaces of the AM metallographic samples did not reveal any pores.

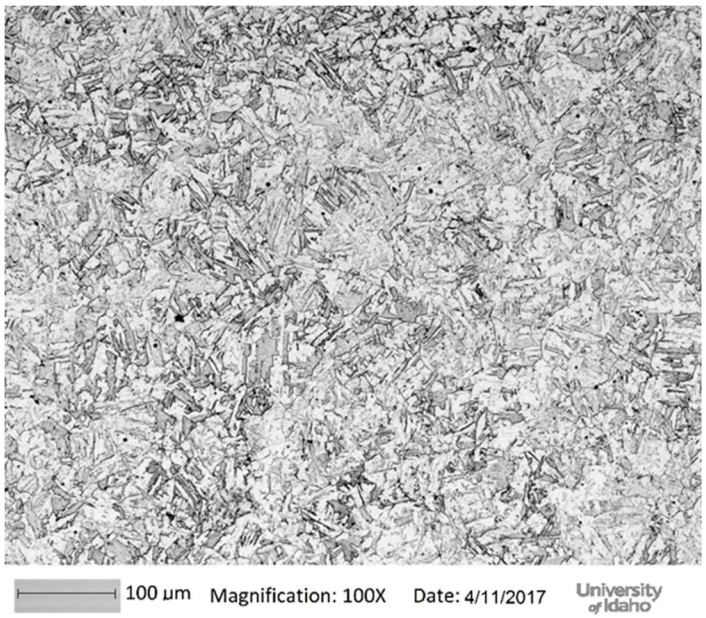

(a)

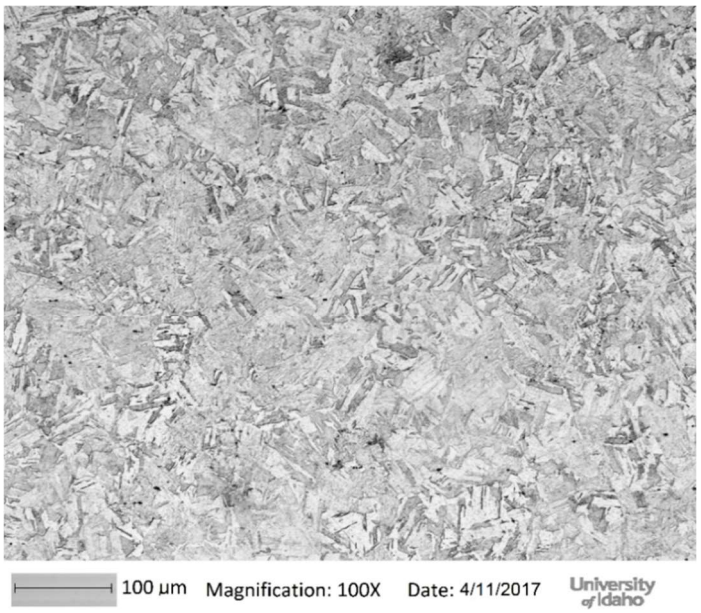

(b)

Figure 2.1 Optical micrographs of the TM 15-5 PH SS samples in the (a) transverse, and (b) longitudinal cross-sections.

However, optical microscopy could not resolve the microstructure of the AM material microstructure and appear to be quite different from the TM material even at higher magnification (500X). Figures 2.2 (a) and (b) show the microstructure of the AM material in the transverse and longitudinal cross-sections, respectively. It appears that the martensitic structure in the AM material is much finer than the TM material.

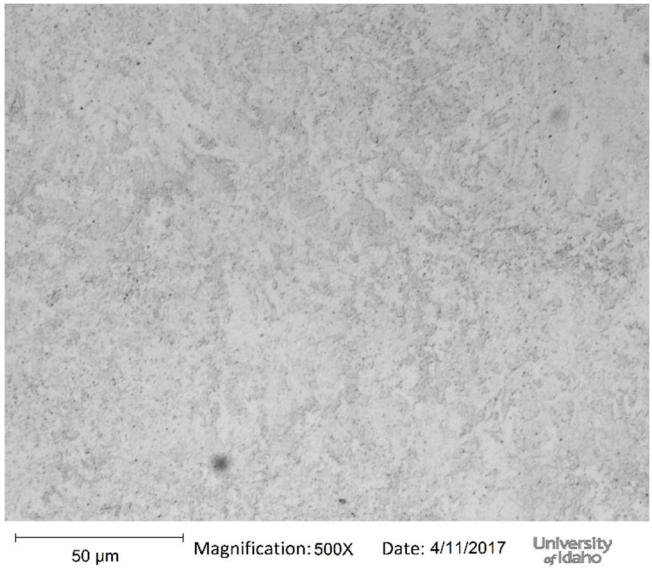

(a)

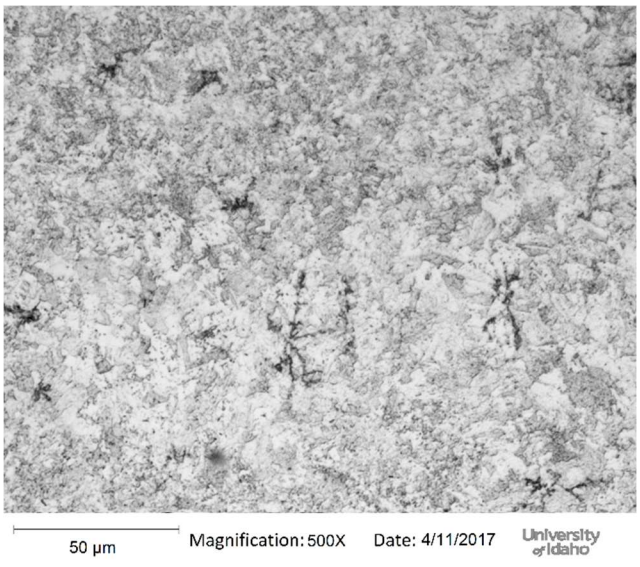

(b)

Figure 2.2: Optical micrographs of the AM 15-5 PH samples in the (a) transverse, and (b) longitudinal cross-sections.

However, the optical microscopy examination did not reveal any fine microstructural details. It necessitated further investigation into the microstructure using characterization tools such as TEM and EBSD. A bright field TEM image of the TM 15-5 PH steel is shown in Figure 2.3(a). Some martensitic elongated, 100-200 nm wide lath structures can be observed. However, other regions of the TM sample did not have consistent lath features. Figure 2.3(b) shows a TEM micrograph of the AM 15-5 PH steel sample. No elongated lath features are observed; rather short packets of narrower lath structures are visible. The microstructure is found to contain high dislocation density. Both specimens appear to contain dislocations and identification of fine particles was difficult because of mottled contrast of the microstructure. One interesting observation was that the AM material contains several spherical particles of 70-90 nm in diameter (some of them shown by arrows in Figure 2.3(b), which were not be observed in the TM material. At this point, their chemical identity is not known and further investigation is ongoing.

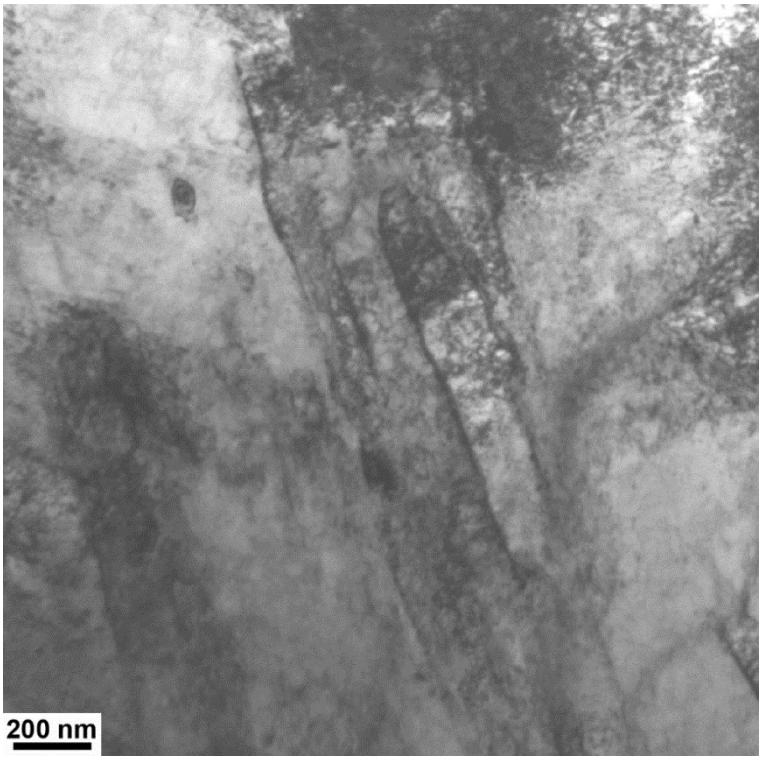

(a)

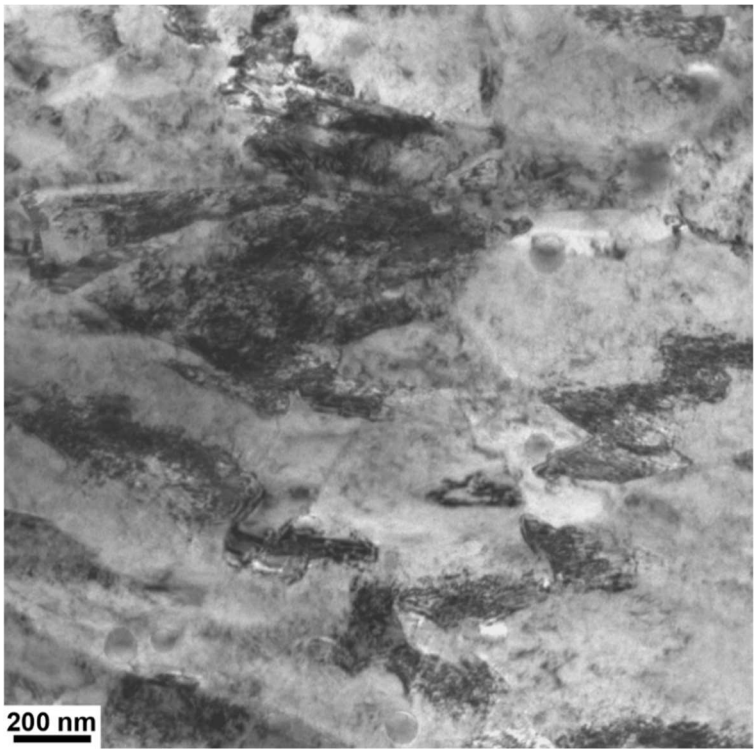

(b)

Figure 2.3: Bright field TEM images of (a) TM and (b) AM 15-5 PH stainless steel.

Figure 2.4 shows a high-magnification TEM image of the AM sample show dislocation activity. It appears that there many nanometric particles which could not be resolved clearly can be seen interacting with dislocations. These could be the coherent copper precipitates. In fact, copper precipitates are expected as 15-5 PH steel contains a maximum of 4.5 wt% copper.

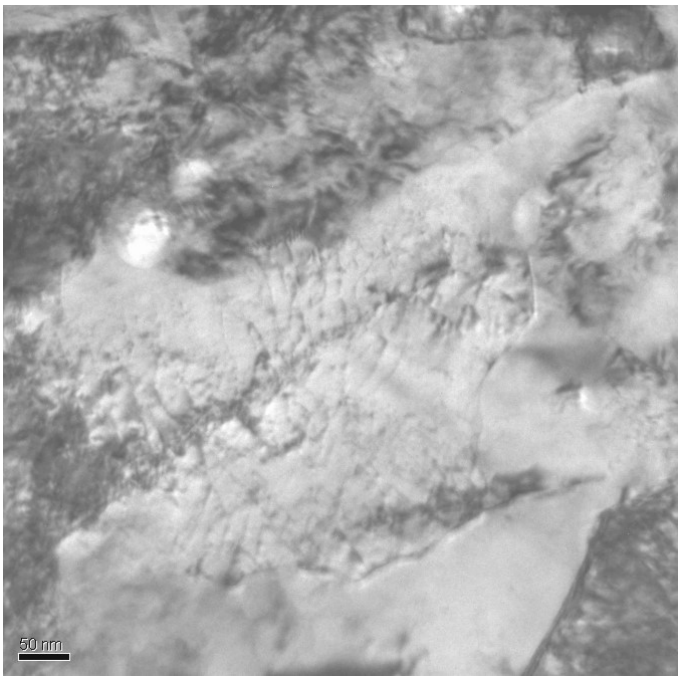

Figure 2.4: A bright field TEM image showing interactions of dislocations with nanometric precipitates in AM 15-5 PH SS.

Figures 2.5 (a) and (b) show the inverse pole figure maps of the TM and AM 15-5 PH SS. Both TM and AM samples show predominantly elongated grains, with TM lath sizes larger than the AM ones. Figure 2.6 shows the grain boundary misorientation distributions of the TM and AM samples. The TM sample has aligned grains with most grains having less than 10^{o} misorientation. In comparison, a portion of grains (about 7%) in the AM sample has a larger grain boundary misorientation around 30^{o}.

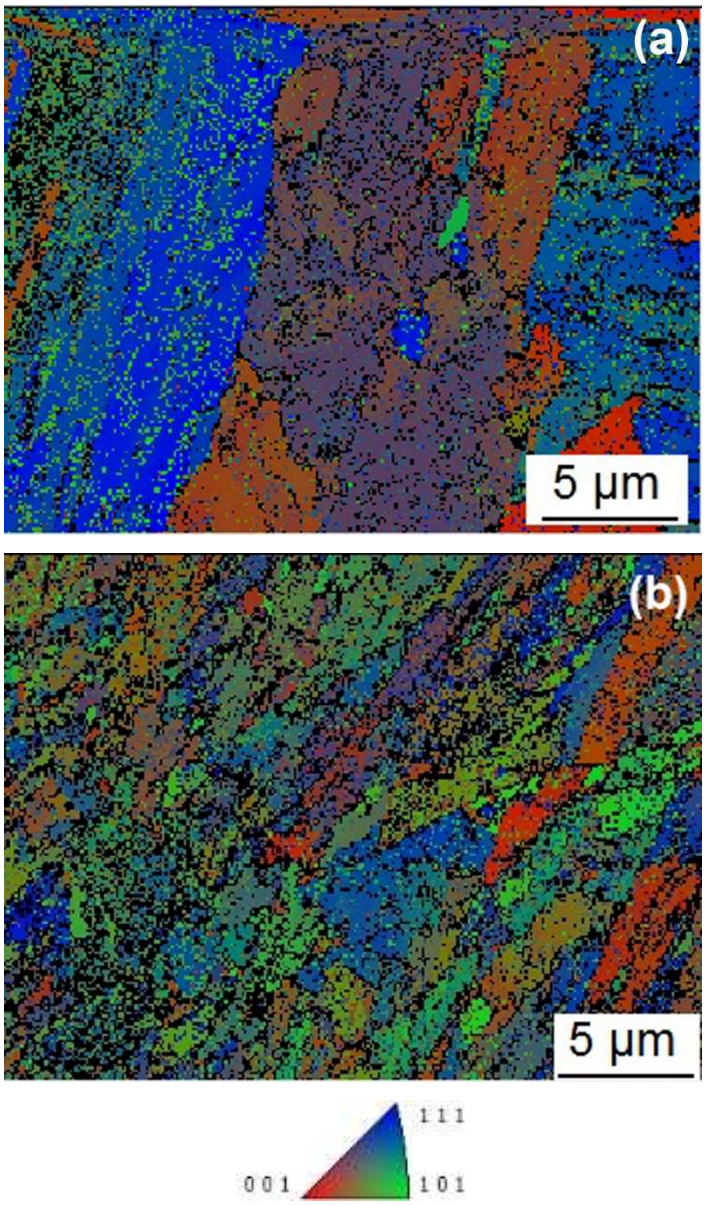

Figure 2.5: Inverse pole figure maps (along the axis of the rod) of (a) the TM and (b) AM 15-5 PH SS materials. Note that both maps show the distribution of other phases. The overlaid dark spots on the BCC map generated are possibly related to phases such as niobium carbide and other particles that could not be indexed.

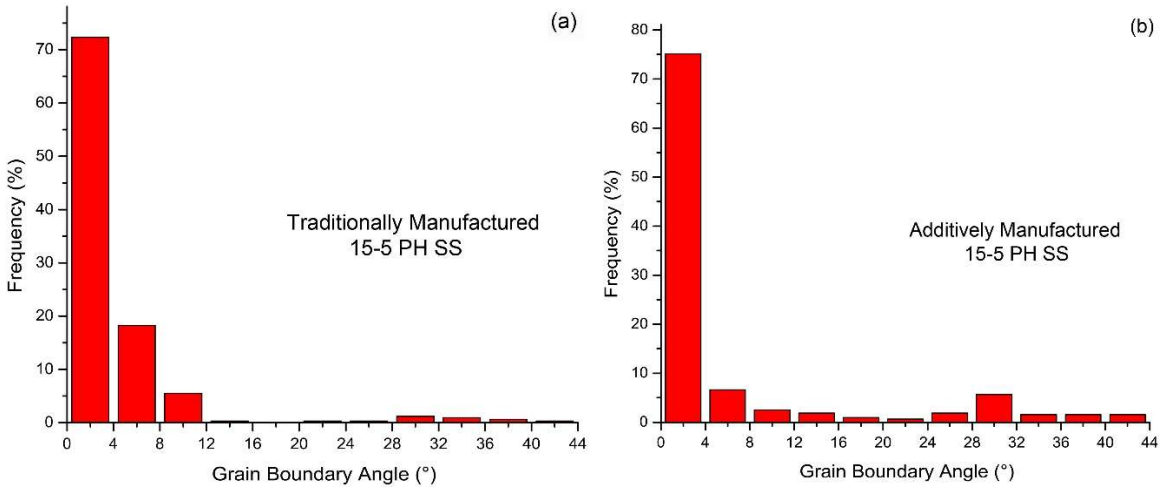

Figure 2.6: Grain boundary misorientation histograms for (a) TM, and (b) AM 15-5 PH SS.

2.3.2. Mechanical Properties

2.3.2.1. Microhardness Testing

Vickers microhardness tests were performed on the transverse and longitudinal cross-sections of both TM and AM samples. The microhardness data are summarized in Table 2.1. The TM material has a lower hardness than the AM material. Furthermore, the hardness data confirm that the AM material is much harder than the TM material.

Table 2.1: Vickers microhardness data of 15-5 PH SS under the TM and AM conditions

	Traditional 15-5 PH		Additively Manufactured 15-5 PH	
	Transverse	Longitudinal	Transverse	Longitudinal
Vickers Microhardness ($HV_{0.5}$)	320 ± 14	330 ± 8	500 ± 12	460 ± 10

2.3.2.2 Tensile Properties

Uniaxial tensile tests were conducted on both the TM and AM materials at a temperature of 593 ºC and a strain rate of 10^{-3} s^{-1}. Figure 2.7 shows the engineering stress – engineering strain curves of the TM and AM materials. Tensile properties such as yield strength, ultimate tensile strength and percentage elongation to fracture are listed in Table 2.2. The yield strength and ultimate tensile strength values are found to be close in both TM and AM materials, which demonstrates quite limited strain hardening capability in both these materials. However, the AM material has almost 30% higher yield strength and 32% higher ultimate tensile strength than the TM material; however, the percentage elongation to fracture and reduction in area (measures of ductility) is found to be relatively low in the AM material compared to the TM material. Room temperature tensile testing at a strain rate of 10^{-3} s^{-1} of AM 15-5 PH SS resulted in yield strength of 850 MPa, ultimate tensile strength of 940 MPa and elongation to fracture of 10%. The room temperature data of the TM 15-5 PH SS used in the present study could not be evaluated because of the limited sample availability. The ASM handbook states that the wrought 15-5 PH SS has yield strength of 1,170 MPa, ultimate tensile strength of 1,310 MPa and elongation to fracture of 10% [12]. But the handbook provides an average data without mentioning which heat treatment. At higher temperature (i.e. 593 ºC), the AM material exhibits only a 7% reduction in yield strength, and a 12% reduction in ultimate tensile strength, while the TM material exhibited 49% and 53% reductions to these parameters, respectively. Thus, it is evident that the microstructural features helped the AM material to better retain strength at the elevated temperature than the TM material.

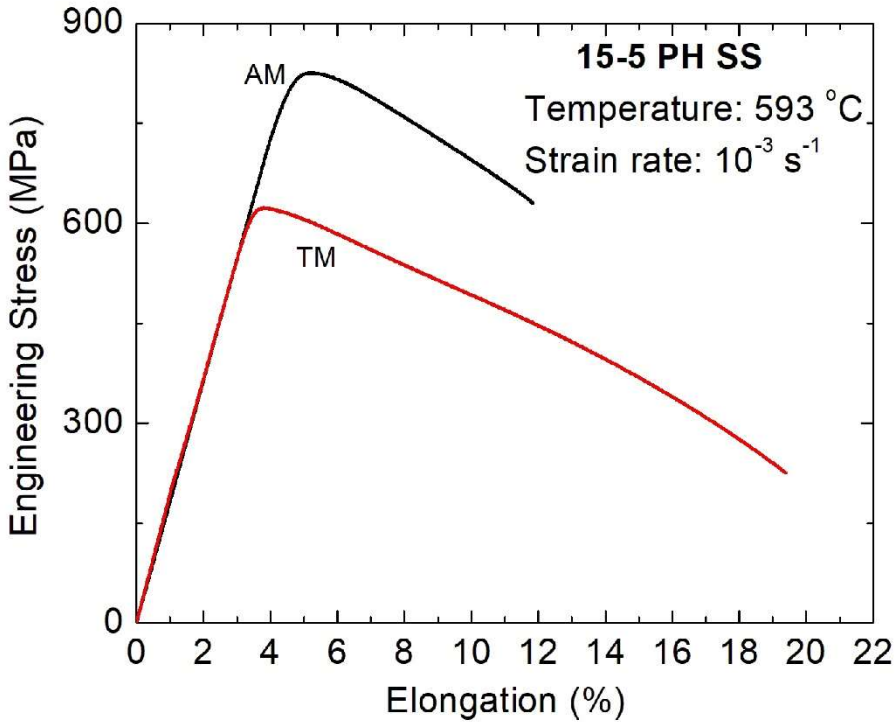

Figure 2.7: Engineering stress – engineering strain curve for 15-5 PH SS of the traditionally manufactured (TM) and additively manufactured (AM) 15-5 PH SS.

Table 2.2: Summary of tensile properties of the TM and AM 15-5 PH SS at 593 °C and a strain rate of 10^{-3} s^{-1}

Tensile Property	**TM**	**AM**
Yield strength (MPa)	610	790
Ultimate tensile strength (MPa)	620	830
Elongation to fracture (%)	19	9
Reduction in area (%)	70	50

2.3.2.3. Comparison of Creep Properties

In this study, creep rupture tests on the TM and AM specimens were conducted at a temperature of 593 °C under an applied stress of 211 MPa. Figure 2.8 shows the corresponding creep curves of the TM and AM materials. Given the short span of these creep tests, they can be basically termed well as stress rupture tests. The creep curves do not exhibit any clear primary and steady state stages presumably because of the high temperature and high stress

level employed during these creep tests. The rupture life for the AM material was found to be 157.2 h as opposed to that of 121.2 h for the TM material. Accordingly, the minimum creep rate for the AM material is measured to be 0.0003%/h and the TM material to be 0.038%/hr. In a wrought and annealed 15-5 PH SS, the minimum creep rate was measured to be 0.015% [13]. Under the creep test conditions, it can be noted that the AM material has superior creep properties compared to the TM material. More creep tests need to be conducted to fully understand the unique creep behavior of the AM materials.

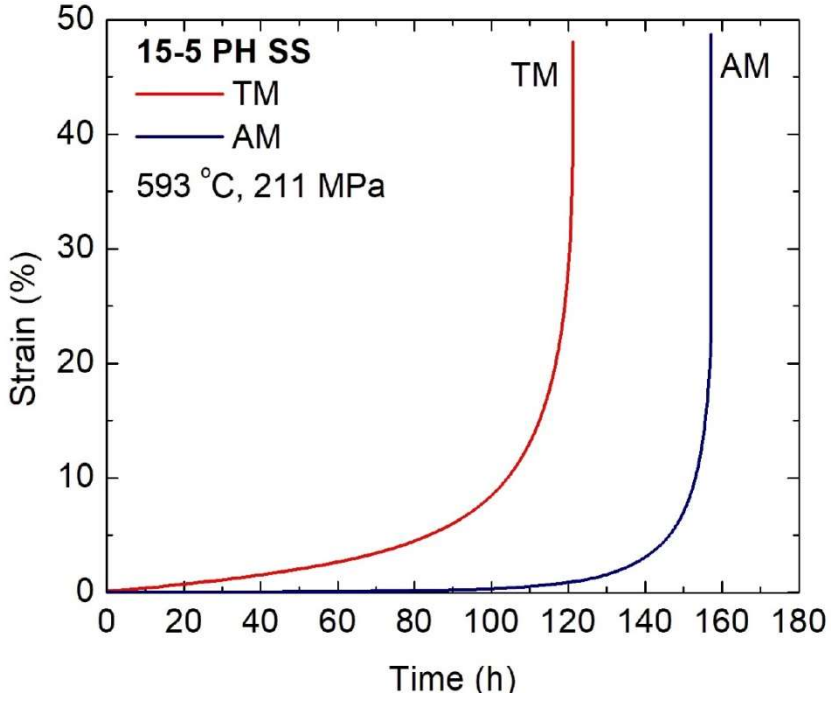

Figure 2.8: Creep curves of TM and AM 15-5 PH SS (tests conditions: temperature of 593 °C and applied stress of 211 MPa)

2.3.2.4. Fractographic Examination

Scanning electron microscopy was performed on the fracture surfaces of both tensile and creep specimens of the AM and TM materials. The purpose of the SEM fractographic study was to examine whether there is any evidence of difference in tensile and creep failure behavior. Figure 2.9 (a) and (b) show the fracture surfaces of tensile and creep specimens of the TM 15-5 PH SS, respectively. The fracture surfaces in the tested tensile and creep

specimens did not reveal any major difference in dimple morphology. The overall roughness of the dimpled surface did not have any special features.

The fracture surface of the AM tensile tested specimen is shown in Fig. 9(c) while the AM creep tested specimen is shown in Fig. 9(d). The AM tensile tested specimen exhibit some interesting features. The surface structure appears to contain wavy, layer-like structure. However, the width of the wave-like features are 25-30 μm. This is probably associated with the size of the powder layers which were used to build the AM rod. Note that the layer size used was about 30 μm as reported in the Experimental section. As we have seen before, the martensite lath structure was about 100-200 nm; so these layers which are much wider than the martensitic laths do not correspond to the features observed on the fracture surface. However, the fracture surface examined for the creep tested AM 15-5 PH SS sample revealed surface topography quite different from the tensile tested AM sample, wherein the wave-like structures are not apparent any more. Greater time at the elevated temperature and low strain rate may have provided opportunities for the material to plastically flow differently influencing the failure mode and creating quasi-dimple features.

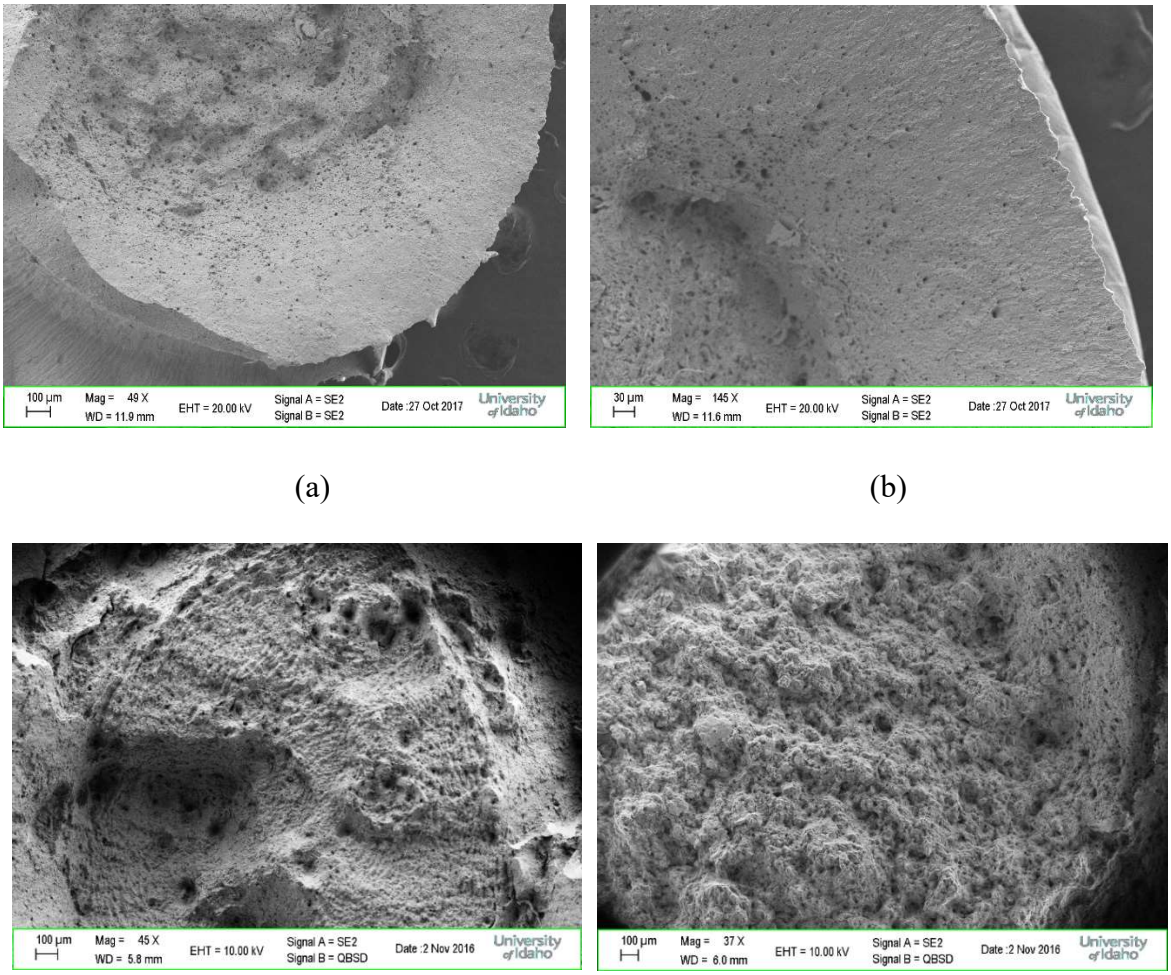

Figure 2.9: SEM secondary electron images of the fracture surfaces of the following 15-5 PH SS specimens tested at 593 ºC: (a) TM – tensile testing; (b) TM – creep testing; (c) AM – tensile testing, (d) AM – creep testing.

2.4 Conclusions

The present study reported some interesting results on the microstructure and mechanical properties of the 15-5 PH SS that was made via AM process (DMLS) in comparison with a TM (wrought) 15-5 PH SS. Microstructural examination of both materials revealed martensitic microstructure. The microstructure of the AM material could not be revealed well by optical microscopy given its fineness. The TEM and EBSD studies revealed somewhat different lath structures with much shorter and narrower laths present in the AM material

compared to the TM material. Some characteristic round shaped particles were also detected in the AM material.

The Vickers microhardness of the AM material at room temperature was found to be greater (by approximately 50%) than that of the TM material. Tensile tests at 593 ^{o}C exhibited a greater strength (by about 30%) for the AM material compared to the TM material while the AM material had a lower ductility (by more than 50%). Furthermore, the creep life of the AM material was found to be greater compared to the TM material when tested at 593 ^{o}C and 211 MPa. At the closing, it can be unequivocally said that the preliminary results obtained from the AM material is quite promising. However, further testing and relevant microstructural analyses need to be conducted to fully understand the high temperature mechanical behavior of the AM material.

Acknowledgement

JZ acknowledges the financial support provided by the Walmart Foundation (project title: Optimal Plastic Injection Molding Tooling Design and Production through Advanced Additive Manufacturing).

Conflict-of-Interest Statement

On behalf of all authors, the corresponding author states that there is no conflict of interest.

References

[1] Frazier W (2014) Metal additive manufacturing: A review. J. Mater. Eng. Perform. 23(6): 1917-1928

[2] Murr LE, Gaytan SM, Ramirez DA, Martinez E, Hernandez J, Amato KN, Shindo PW, Medina FR, Wicker RB (2012) Metal Fabrication by Additive Manufacturing Using Laser and Electron Beam Melting Technologies. J. Mater. Sci. Technol. 28(1):1-14

[3] Rafi HK, Pal D, Patil N, Starr, TL, Stucker, B. (2014) Microstructure and mechanical behavior of 17-4 precipitation hardenable steel processed by selective laser melting. J. Mater. Eng. Perform. 23: 4421-4428

[4] Fachhini L, Vincente N, Lonardelli I, Magalini E, Robotti P, Molinari A, (2010) Metastable austenite in 17–4 precipitation-hardening stainless steel produced by selective laser melting. Adv. Eng. Mater. 12 (3): 184-188.

[5] LeBraun T, Nakamoto T, Horikawa K, Kobayashi H, Effect of retained austenite on subsequent thermal processing and resultant mechanical properties of selective laser melted 17-4 PH stainless steel, Mater. Des. 81 (2015) 44-53

[6] AlMangour B, Yang J-M (2017) Understanding the deformation behavior of 17-4 precipitate hardenable stainless steel produced by direct metal laser sintering, Int. J. Adv. Manuf. Technol. 90: 119-126

[7] Spierings AB, Starr TL, Wegener K (2013) Fatigue performance of additive manufactured metallic parts. Rapid Protyp. J. 19(2): 88-94

[8] Rafi HK, Starr TL, Stucker BE (2013) A comparison of tensile, fatigue and fracture behavior of Ti-6Al-4V and 15-5 PH Stainless Steel parts made by selective laser melting. Int. J. Adv. Manuf. Technol. 69 (5-8): 1299-1309

[9] Buchanan C, Matilainen V-P, Salminen A, Gardner L (2017) Structural performance of additive manufactured metallic materials. J. Construc. Steel Res. 136: 35-48.

[10] Lee H, Lim C H J, Low M J, Tham N, Murukeshan VM, Kim YJ (2017) Lasers in Additive Manufacturing: A Review. International Journal of Precision Engineering and Manufacturing 4(3):307-322.

[11] Khaing MW, Fuh JYH, Lu L (2001) Direct metal laser sintering for rapid tooling: processing and characterization of EOS parts. J. Mater. Process. Technol. 113: 269-272

[12] ASM Handbook (1993), Volume 1: Properties and Selection: Irons, Steels, and High-Performance Alloys 1993, ASM International, Materials Park, OH

[13] Deel OL, Mindlin H (1972) Engineering Data on New Aerospace Structural Materials, Technical Report, AFML-TR-71-196.

Chapter 3 Preliminary Examination of the Effect of Traditional Heat Treatments on the Microstructure and Hardness of Additively Manufactured 15-5 PH Stainless Steel

Abstract

In the present study, 15-5 PH stainless steel (SS) was produced via an additive manufacturing (AM) technique known as Direct Metal Laser Sintering (DMLS). The microstructure and microhardness of the AM alloy were compared with and without a solution heat treatment before an aging heat treatment, and with a heat treated traditionally manufactured (TM) 15-5 PH SS. Vickers microhardness values of the solution heat treated and TM 15-5 PH SS were found to be in good agreement after most aging treatments, while the non-solution heat treated 15-5 PH SS exhibited a 10-30% higher microhardness than either. Transmission Electron Microscopy (TEM) examination of the samples showed that the solution heat treated condition of the AM material and the traditional material exhibited precipitates of similar sizes, while the non-solution heat treated material had precipitates of approximately 40% smaller size.

3.1 Introduction

In recent times much research has been ongoing surrounding the Additive Manufacturing (AM) or 3-D printing of metallic materials. AM has been defined by the ASTM as the "process of joining materials to make parts from 3D model data, usually layer upon layer, as opposed to subtractive manufacturing and formative manufacturing methodologies" [1]. While AM has been around since the late 1980's, in recent years the industry has shown rapid growth as both consumer grade, polymer-based AM machines and industrial grade machines become more and more affordable, and projections show $8 billion in material sales are possible by 2025 [1].

The rapid growth of the industry centered around this new approach to manufacture has seen said growth because it brings to the table a multitude of benefits and opportunities. AM parts reach their final shape in a single manufacturing step, using less energy and with less waste material than traditional methods, and new vistas of part geometries unachievable by traditional manufacturing (TM) methods are possible. Further, AM machines are compact, easy to add to a machine shop, and would enable quick manufacture of any part necessary to the operation of any given machinery. AM machines promise a shortening of supply lines, a

reduction in spare inventory, and a reduction in potential downtime for repairs. While economies of scale may always ensure that the largest mass quantities will be cheapest to manufacture in the traditional way, small runs of parts and prototypes are already cheap and easy to realize via AM technology. As the hurdles currently facing AM are surmounted, the size of an economically viable run of parts from an AM machine can be expected to rise considerably.

There are several hurdles that are currently preventing widespread adoption and use of AM parts. The main challenges faced in the AM field today can be categorized into a few main issues. Firstly, AM materials undergo different processes to reach their final shape than their TM counterparts would experience. There is a definite difference in microstructure because of this, and the effect this difference in microstructure has on engineering properties need to be carefully evaluated, to ensure that any parameter that might be designed around is as accurate as possible [3]. Further, process control and process mapping during the AM operation itself is also lacking. Currently, leftover powder used in powder bed systems is reused, but several studies have seen a difference in the parts produced by this powder [3]. In situ process monitoring and feedback control also lacks the robustness needed to ensure produced parts are all equivalent [3]. Finally, quality control of AM parts is a human labor-intensive operation. Some method of qualifying AM parts without this labor is necessary to expand AM produced material past extremely small runs of parts and prototypes [3].

Currently, there are multiple AM techniques with at least one economically viable machine on the market. One of these techniques is Direct Metal Laser Sintering (DMLS) [2] [4]. The DMLS process requires a high-powered laser, and feedstock powder. The feedstock powder of choice is loaded into the machine and spread in a thin layer over an entire powder bed in the machine via a rake of a certain type. The laser is then used to selectively deliver the energy required to fuse the powder in a layer as described by the CAD file. After the layer is fused, the powder bed is lowered, another layer is spread across the fused one, and the process repeats until the final layer has been fused. After the part is complete, the unfused powder is collected for reuse, and the part goes on to such post processing as deemed necessary. These post processing treatments can include surface polishing, as well as post processing heat

treatments to either relieve residual stress caused by high temperature gradients during manufacture, or to achieve the required material characteristics.

One alloy of commercial importance is 15-5 PH stainless steel that has been processed via DMLS. 15-5 PH SS is a martensitic precipitation hardening stainless steel used in multiple industries, such as the aerospace, chemical, and food processing industries for its high strength, and good corrosion resistance. As a precipitation hardening steel, heat treatment is an important part of the manufacturing process, allowing its material characteristics to be tailored to the application, after the final required shape is obtained. Due to the effects AM has on 15-5 PH stainless steel, the heat treatment schedules used for TM 15-5 PH stainless steel may need to be adjusted [5]. While some previous work has been done in this area, further research is needed to ensure that heat treated specimens have the proper material characteristics. The current study is an examination of the differences between the effects of heat treatment on AM 15-5 PH SS and its traditionally manufactured counterpart.

3.2 Experimental

AM samples were prepared by an EOSINT M270 (EOS GmbH Electro Optical Systems, Germany) machine equipped with a 200 W single mode Yb fiber laser with a wavelength of 1070 nm. Samples were manufactured with the laser power at 170 W, at a scanning speed of 1250 mm/s in continuous wavelength mode, with a spot size of approximately 50 μm, with a hatch spacing set to 1000 μm, and layers of 30 μm thickness. Argon was used as the nonreactive atmosphere.

EOS Stainless Steel PH1, a 15-5 PH powder manufactured via gas atomization was used as the feed stock. This powder adheres to standard 15-5 PH chemistry, with a nominal composition of Fe (balance), Cr (14 – 15.5 wt%), Ni (3.5 – 5.5 wt%), Cu (2.5 – 4.5 wt%), Mn (max. 1 wt%), Si (max. 1 wt%), Mo (max. 0.5 wt%), Nb (0.15 - 0.45 wt%), and C (max. 0.07 wt%). Cylindrical rods of 15 mm diameter × 90 mm length were printed to be sectioned later. Post-processing consisted solely of a low temperature stress relief heat treatment, which was carried out at a low enough temperature so as not to alter the microstructure or mechanical properties. The TM 15-5 PH SS was acquired from the marketplace as round bar stock of 25 mm diameter. Unfortunately, the exact as received heat treatment condition of the TM bar is not known.

Heat treatment was carried out in a Micropyretics Heaters International horizontal tube furnace capable of reaching 1550 °C. Heat treated samples were of three different types. 'A' type samples were produced via AM, then they were given the standard solution heat treatment for 15-5 PH, 30 minutes at 1040 °C followed by air cooling to room temp, and subsequently they underwent a standard aging treatment for 15-5 PH. 'B' type samples were also produced via AM, then given the same standard 15-5 PH aging treatment as the 'A' type (without the solution heat treatment.) 'C' type samples were of the TM bar stock, and they were again given the standard solution heat treatment, followed by the same standard aging heat treatment as the other samples.

Table 3.1: Standard industrial heat treatments

Heat Treatment Name	Time and Temperature
H900	1 hr at 480 °C
H925	4 hrs at 496 °C
H1025	4 hrs at 552 °C
H1075	4 hrs at 580 °C
H1100	4 hrs at 593 °C
H1150	4 hrs at 621 °C
H1150-1150	4 hrs at 621 °C, air cool, 4 hrs at 621 °C
H1150-M	2 hrs at 760 °C, air cool, 4 hrs at 621 °C

Standard aging heat treatments for 15-5 PH specimens can be seen in Table 3.1. All heat treatments are followed by air cooling the heat-treated material. The heat treatments are named for the Fahrenheit temperature they are carried out at. These heat treatments are used to tailor the hardness and ductility of the

Samples for microhardness, transmission electron microscopy (TEM), and X-ray diffraction XRD were sectioned via diamond wafering blade, and hot mounted in black phenolic mounting powder with a Pace Technologies Mounting Press at 170 °C, if mounting was deemed necessary. These samples were then ground with silicon carbide grinding paper

from 250 grit up to 1200 grit and polished to a final surface finish with 0.1 μm alumina polishing solution and a polishing cloth.

Vickers microhardness tests were performed on the samples using a Leco LM100 Microhardness Tester with a load of 0.5 kg_f with a standard dwell time of 15 s. Each sample was tested six separate times at random locations to ensure a decent average.

Sections of metal from select samples were thinned to 50-100 μm, punched into 3 mm diameter disks, and jet polished using an electrolyte of composition 20 vol% nitric acid and 80 vol% methanol in a Fischione twin-jet electropolisher at about -35 ºC. The TEM specimens were examined using a JEOL 2010J TEM at an accelerating voltage of 200 kV. Energy dispersive spectroscopy (EDS) system available within the TEM was used to obtain local composition of precipitates in the samples.

3.3 Results

3.3.1 Vickers Microhardness Data

The Vickers microhardness results are listed in Table 3.2. Concurrently with Vickers microhardness data collection, optical micrography was attempted on the samples, but this line of inquiry did not produce appreciable data. Due to low availability of samples, the Vickers microhardness data were used to choose a heat treatment of particular interest for TEM studies.

Figure 3.1 shows the Vickers microhardness data for the majority of the standard heat treatments. It should be noted that the H900 heat treatment requires the material be held at 480 °C for only 1 hour, as opposed to the other heat treatments displayed, which require 4 hours at temperature. Additionally, the H1150-1150 and H1150-M heat treatments are not included in the plot, as these aging treatments are more complex than the others. As seen in Figure 3.1, the H1025 heat treatment showed the greatest similarity between the ‘A’ and ‘C’ sample sets and the greatest difference between these and the ‘B’ sample sets, as well as being the end of a plateau for the ‘B’ type samples.

Figure 3.1 also shows the relative similarity between the hardness of the ‘A’ and ‘C’ type samples. As can be seen, the hardness values of these two samples have remarkable

agreement, indicating that the microstructures of these samples are very similar. While further examination of other mechanical properties is needed for further confirmation, the addition of a standard solution heat treatment may cause AM 15-5 PH SS to act near identically to its TM counterpart.

Table 3.2: Vickers microhardness of heat-treated and as-received samples.

	A Samples		B Samples		C Samples	
Heat Treatment	VHN	Std. Dev	VHN	Std. Dev	VHN	Std. Dev
H900	438	9	486	5	436	4
H925	410	4	470	12	424	21
H1025	374	7	474	4	374	12
H1075	366	5	448	11	366	5
H1100	365	16	448	5	357	17
H1150	341	12	407	18	331	3
H1150-1150	318	17	414	4	318	3
H1150-M	361	7	327	11	340	6
As-Received Samples						
As-Rec. AM	500	12				
As-Rec. TM	320	8				

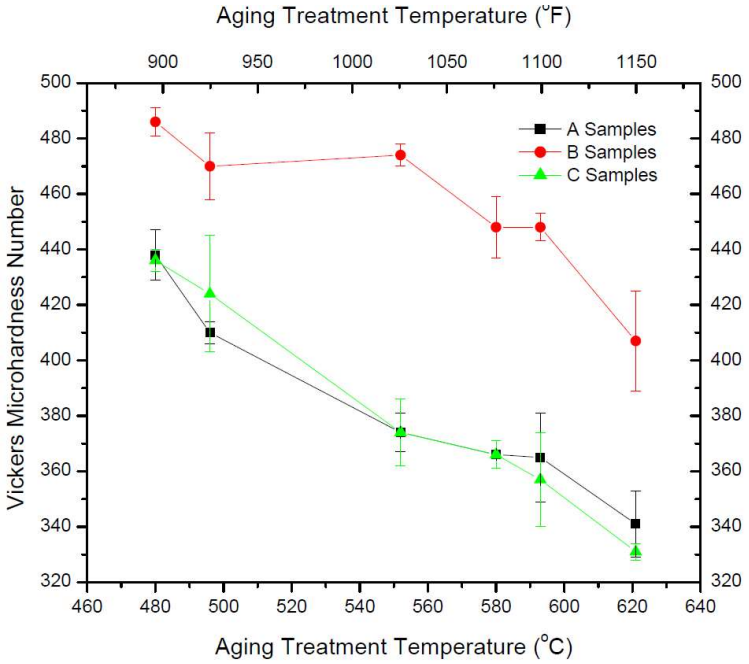

Figure 3.1: The effect of heat treatment temperature on Vickers microhardness in 15-5 PH SS. Of the heat treatment conditions shown, only H900 (i.e. 480 °C) occurred for a shorter period of time, 1 hr, versus 4 hrs for all the other heat treatments shown here.

3.3.2 TEM Examination

Because of the large number of samples, only three aged samples (H1025 A, H1025 B, and H1025 C) were examined. In TEM examination, all three samples showed clear martensitic lath structures. Figure 3.2 shows a bright field TEM image of Sample H1025 A, in which can be seen a set of martensitic formations which may exhibit the directional bias expected from an AM metal, as discussed by Zhang et al [4]. This directional bias is caused by the thermal gradient produced when the laser tracks across the powder while fusing the sample [4]. No further clear martensitic structures showing the directional bias could be detected in the viewable sample area. In Figure 3.3, the bright field image of the H1025 B sample exhibits several clear martensitic laths, but none clearly displayed the v-oriented laths in the same direction as those in Figure 3.2, hence those seen in the 'A' sample may be coincidental. Figure 3.4 shows martensitic laths in sample H1025 C, but these seemed rarer in the 'C' type sample than the previous two, and they were not as clear as those observed in the 'A' and 'B' type samples.

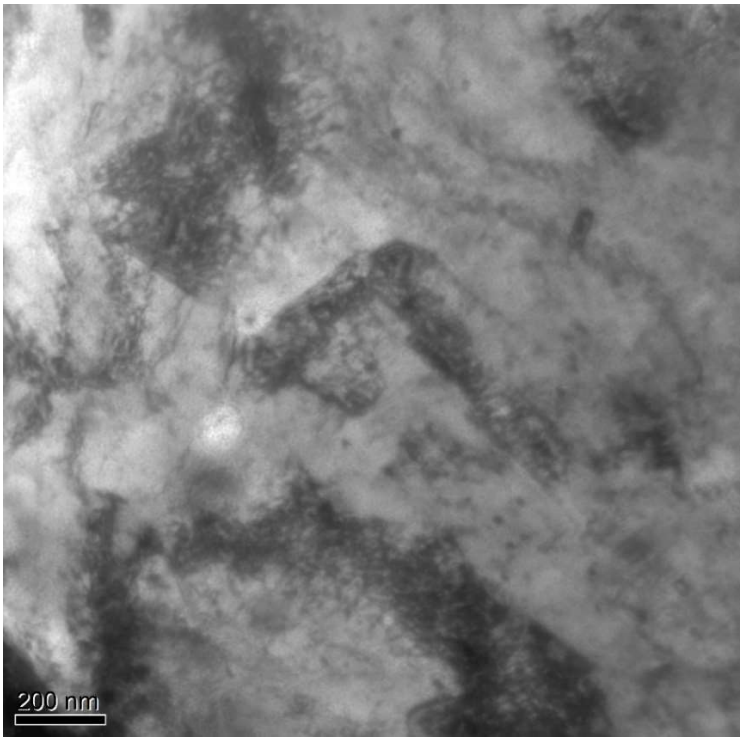

Figure 3.2: TEM image of sample H1025 A showing martensitic structure

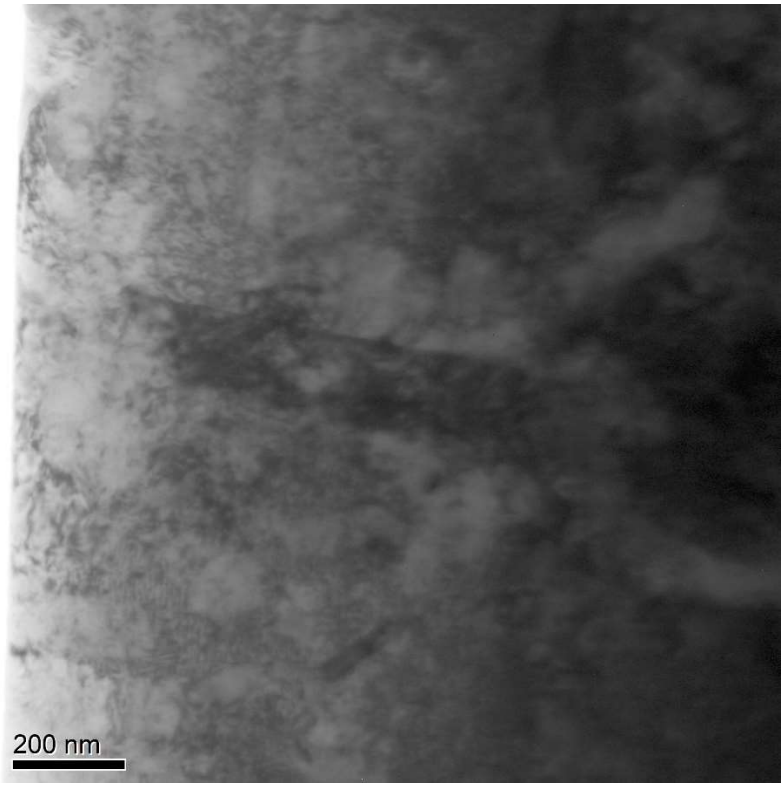

Figure 3.3: TEM image of sample H1025 B showing martensitic structure

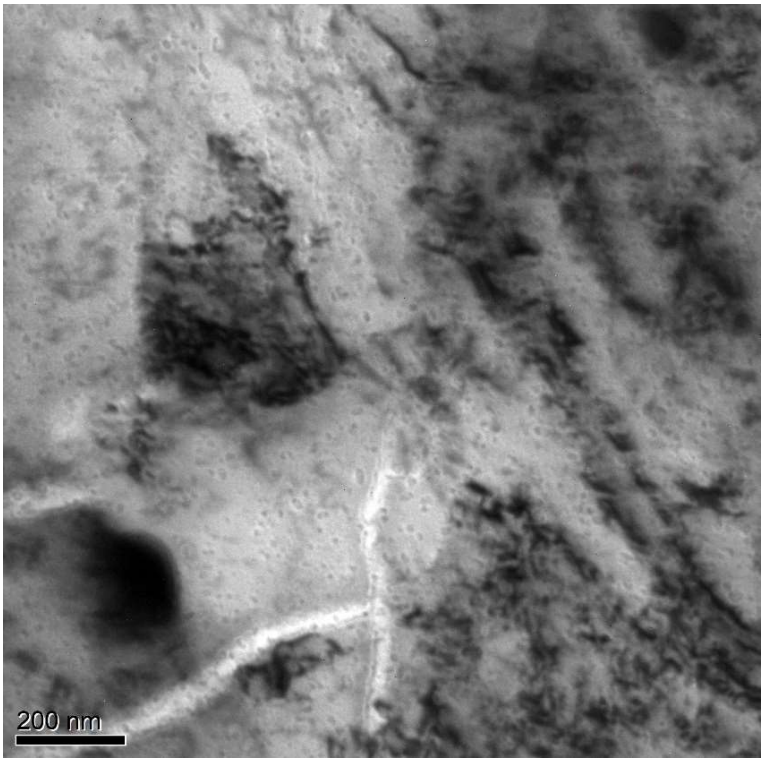

Figure 3.4: TEM image of sample H1025 C showing martensitic structure

Figures 3.5, 3.6, and 3.7 show the nano-scale precipitates in 15-5 PH SS. Previous research has shown that the precipitates in 15-5 PH are expected to be nearly pure copper [6] [7]. EDS results of the H1025 A sample shown in Figure 3.5 show a large copper response in the selected area, enough to confirm these precipitates to be the pure copper precipitates. The EDS results of H1025 B seen in Figure 3.6 also exhibits an increased copper response from the area and so can be assumed to be the pure copper precipitates as well. The EDS results of Figure 3.6 show a strong Ti peak, which may be contamination from a previous run of the manufacturing machine, or an additive used to capture other contaminants. Figure 3.7 shows the results of the H1025 sample C, which exhibits a lower copper reading than the other two samples, but still a greater reading than expected from the matrix. The lower copper response seen in Figure 3.7 may be due to the increased presence of Cr carbide precipitates, which are known to occur sporadically in the original microstructure as M_7C_3 type particles and known to form as $M_{23}C_6$ carbides as aging occurs [6] [7]. In addition, the morphology of the precipitates seen in Figure 3.7 clearly shows the Ni, Mn and Si enriched shell, described by previous research, while the AM samples do not clearly exhibit this shell [7].

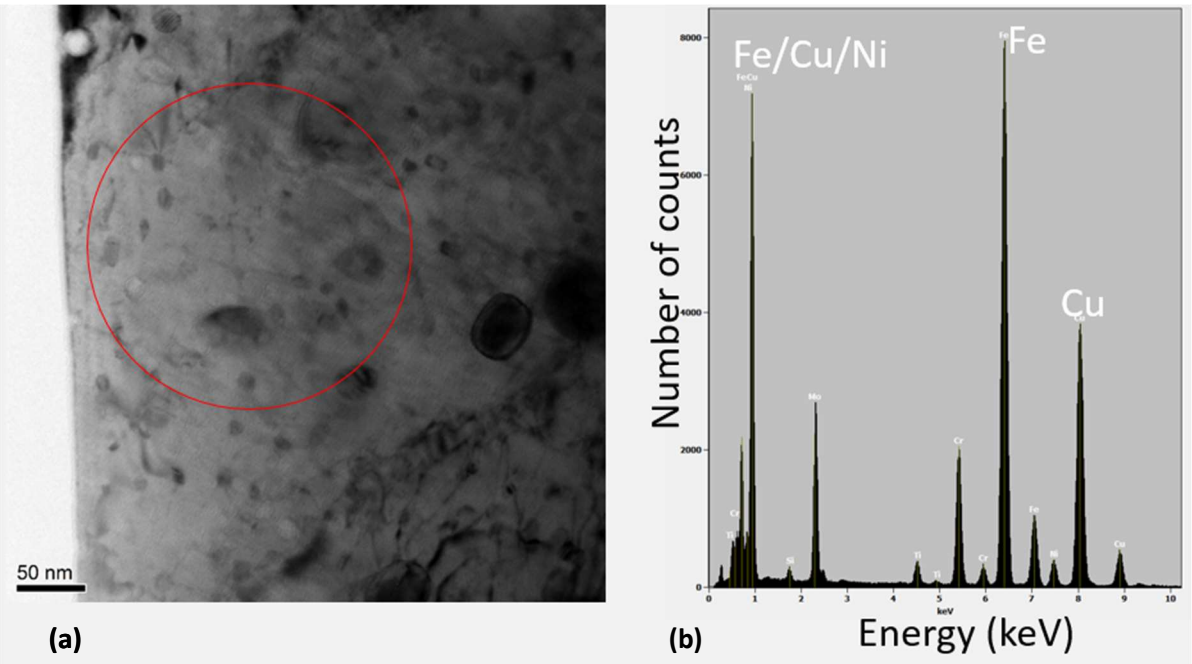

Figure 3.5: (a) TEM image of precipitates in Sample H1025 A. The red circle shows the approximate EDS area. (b) The EDS spectrum of the area shown by the red circle in (a).

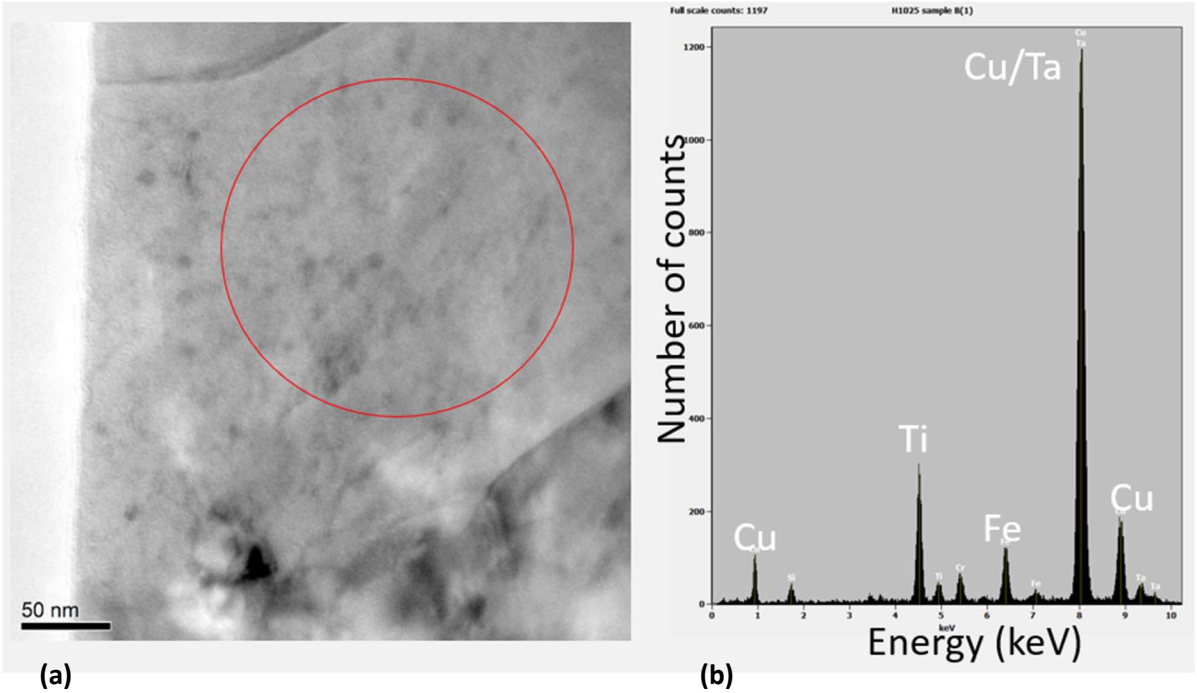

Figure 3.6: (a) TEM image of precipitates in sample H1025 B. The red circle shows the approximate EDS area. (b) The EDS spectrum of the area shown by the red circle in (a).

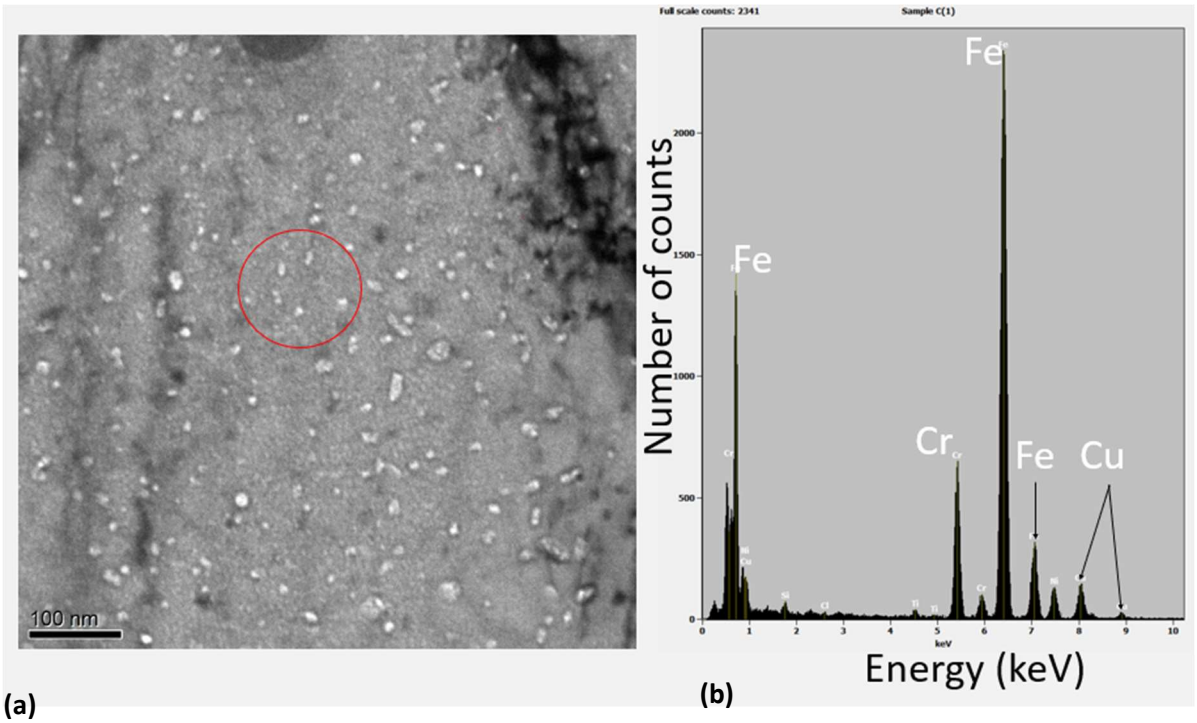

Figure 3.7: (a) TEM image of precipitates in sample H1025 C. the red circle shows the approximate EDS area. (b) The EDS spectrum of the area shown by the red circle in (a)

Histograms of the particle sizes measured from the TEM micrographs of the samples can be seen in Figures 3.8-3.10. In sample H1025 A, the precipitates were sized in the 7-11 nm range, which is similar, though slightly larger than the particles seen in sample H1025 C, which were in the 6-9 nm range. In both 'A' and 'C', the size of the copper precipitates was mostly of 9 nm mean diameter. In sample H1025 B, the precipitates showed a preference for sizes ranging from 5-7 nm, as can be seen in Figure 3.9. The mean particle diameters determined in the samples are listed in Table 3.3. H1025 A exhibited the largest average particle diameter. Further research is needed to determine the exact reason for this increase range. In the measurement, really fine particles of copper were included excluding the larger carbide particles.

Table 3.3: Mean particle diameter of heat-treated samples

Sample Type	Mean Particle Diameter (nm)
H1025 A	9.2
H1025 B	5.6
H1025 C	8.4

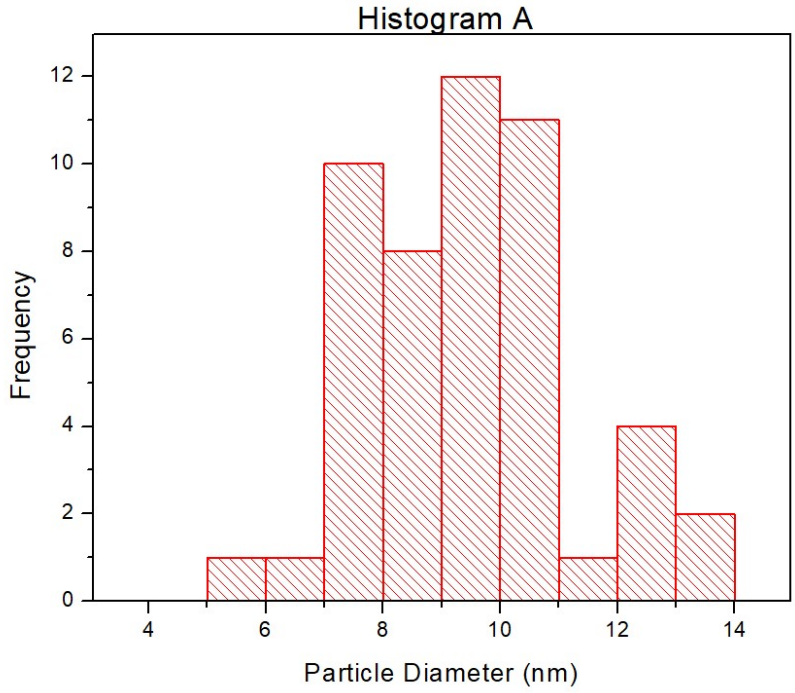

Figure 3.8: Histogram of Cu particle size distribution in Sample H1025 A

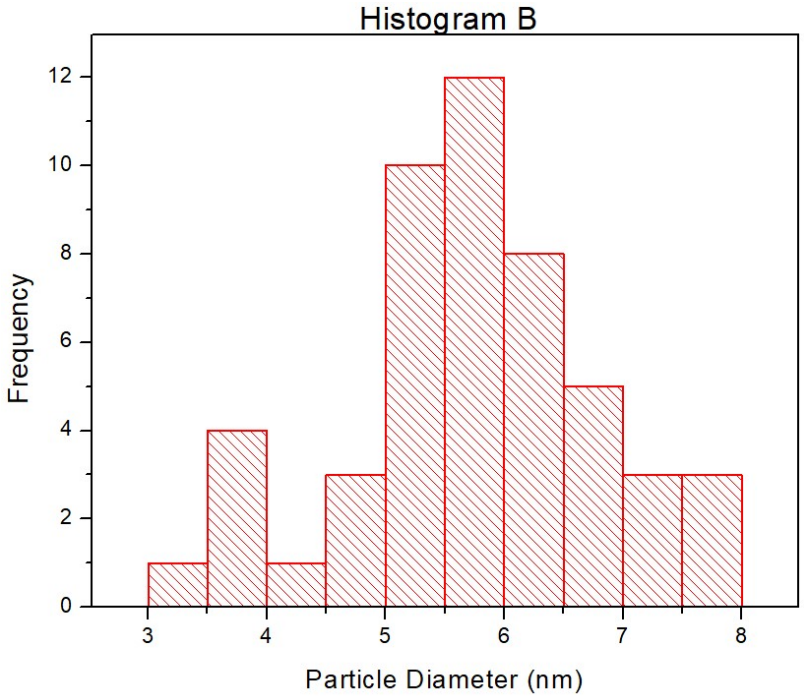

Figure 3.9: Histogram of Cu particle size distribution in Sample B

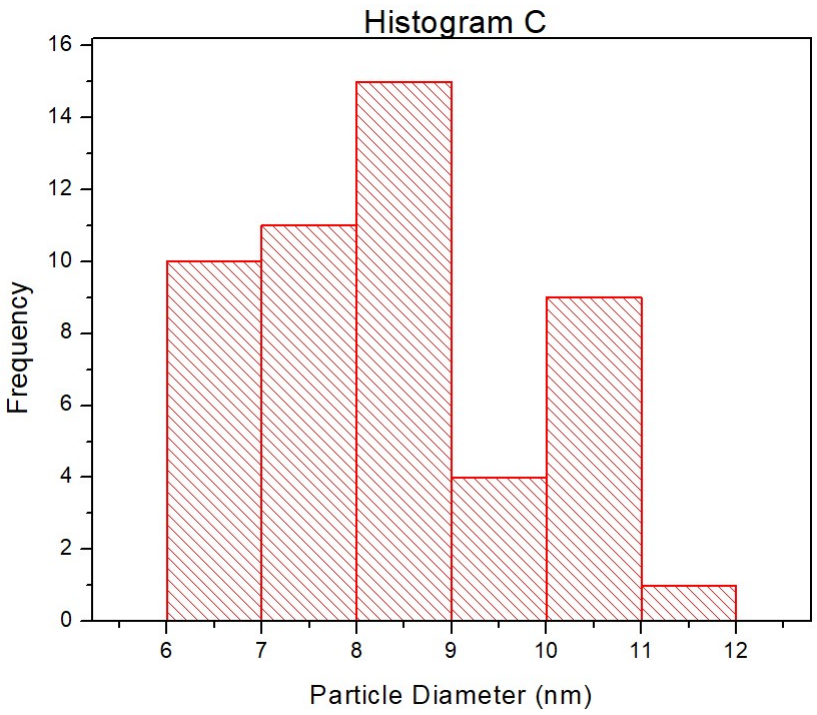

Figure 3.10: Histogram of Cu particle size distribution in Sample C

3.4 Discussion

3.4.1 Effect of the Solution Heat Treatment

An investigation into the martensite to austenite formation mechanism in 15-5 PH SS was completed recently [8]. In this research, it was suggested that this transformation is diffusion controlled, and highly sensitive to the heating rate the material underwent [8]. In their study, Brandl et al. determined that the austenite transformation start temperature (A_{c1}) is approximately 720 °C while the austenite transformation completion temperature (A_{c3}) should be around 850 °C for 15-5 PH SS [8]. Additionally, they determined both the A_{c1} and the A_{c3} temperatures are both dependent on heating rate [8]. As the heating rate increases, the A_{c1} temperature will decrease, while the A_{c3} temperature will increase [8]. Further, the austenite formation shows a two-step composition change. The first step involves nickel enrichment in the austenite, while chromium is depleted in the austenite phase [8]. The second step involves the homogenization of the nickel and chromium concentrations throughout the austenite matrix after austenite has completed its formation [8]. The reverted austenite is

expected to nucleate on low angle grain boundaries between laths in acicular formation of the same size as the martensitic laths [8].

Based on this information, inferences can be made as to what happened to the microstructure of the H1025 A sample during solution heat treatment. While no heating rate data was collected, because the sample was placed into the furnace after the required 1040 °C temperature was reached, it can be assumed the heating rate was near the maximum possible. Therefore, full, or nearly full, reversion to austenite should have taken place. However, as the kinetics of the second stage of the martensite to austenite transformation is diffusion controlled, currently it is not possible to determine with certainty the condition of the homogenization process. Due to the differences detected with regards to particle diameter range and Vickers microhardness between the H1025 A sample and the H1025 C sample, some inhomogeneities are expected to exist.

Upon air cooling of the H1025 A sample, it can be expected that the sample will act nearly identically to TM 15-5 PH. An estimated martensite start temperature (M_s) can therefore be calculated using the weight percent of the alloying elements and Equation 3.1 given by Ishida [9].

$$M_s(°C, wt.\%) = 545 - 330C + 2Al + 7Co - 14Cr - 13Cu - 23Mn - 5Mo - 4Nb - 13Ni - 7Si + 3Ti + 4V + 0W \quad (3.1)$$

Via this equation, the M_s temperature of 15-5 PH ranges between 215 °C and 141 °C depending on the composition. According to the literature, M_s temperatures approximately 200 K above room temperature indicate a sufficient driving force for martensitic transformation at room temperature [10]. While there is no real martensite finish temperature (M_f), it is often defined as the temperature at which the microstructure is 95% martensite [11]. The author is unaware of any kinetics models that can be used to calculate the volume fraction of martensite that can be used on stainless steels, but 15-5 PH SS has been experimentally determined to be approximately 98% martensite at room temperature [7]. It can therefore be assumed that after cooling, the microstructure of sample H1025 A will closely resemble that of the TM material in the same condition. Accordingly, after solution heat treatment, the H1025 A sample most likely exhibited a lath martensite structure with high dislocation density

and an effective grain size similar to that of the TM material [6] [7]. Niobium carbides of 200 nm size or greater most likely also exist in this microstructure, but these carbides exist to trap carbon content, and are not expected to have any significant strength contribution [6] [7]. Further examination of the AM sample after the solution heat treatment is required to determine the adequacy of this assumption.

3.4.2 Effect of Aging Heat Treatment

Previous research into the effect of the aging heat treatments on the microstructure of 15-5 PH SS alongside the current data can again be used to infer what effect the aging heat treatments are having on the samples in this study.

The effect of an aging heat treatment on 15-5 PH SS is directly related to the time and temperature at which the treatment occurs [6] [7] [12]. As has been covered, the primary effect of the aging treatment is to precipitate fine, widely dispersed copper particles to increase the strength of the material. While there is no enumerated minimum temperature value, lower temperature kinetics make temperatures below around 450 °C push the aging time required to reach peak hardness to 3 hours or more [12]. Thus, 450 °C is an acceptable minimum temperature to consider in discussion of the aging effect.

Another aspect important to consider pertaining to the copper precipitates is the relationship between their size and the effect they have on the matrix. As they grow, the copper particles in 15-5 PH go through several crystalline structures, as described in the literature. Copper precipitates have been shown to form with a coherent BCC structure [6] [7]. As they grow, they transform through several intermediate microstructures of decreasing coherency with the matrix, before transforming into the FCC structure expected of pure copper [6] [7]. While explanation of the exact structures is beyond the scope of this paper, for this discussion it is sufficient to note the critical sizes at which these transformations occur. The particles will precipitate as coherent BCC particles, and their crystalline structures will transform as their size increases. These transformations occur when particle diameters are approximately 4 nm, 10 nm, and 20 nm. Each transformation reduces the coherence of the particles, until they transform into incoherent FCC particles at 20 nm [6] [12].

Aging is also known to have additional effects on the overall microstructure of 15-5 PH SS. At higher aging temperatures, 500-700 °C, martensite tempering will occur [13] [14]. Tempering of martensite involves relieving internal stresses in the matrix, increasing its ductility at the expense of hardness [13] [14]. Additionally, dislocation cells, areas of lower dislocation density defined by three dimensional areas of high dislocation density that act as cell 'walls', will develop [13]. Austenite reversion is also known to happen at these temperatures [13]. Austenite is a softer phase than martensite and increasing volume fraction will also improve ductility and reduce hardness [13][14].

Knowing these properties, the effect of aging in differing temperature ranges can be discussed. In the temperature region of 450 °C to around 520 °C, the copper particles can be quickly precipitated to the value required for maximum effect [12]. Peng et al. [12] showed that the maximum hardness could be quickly achieved in this temperature regime and was stable out past 8 hours. Microstructural studies done at these temperatures show copper precipitates having approximate sizes of 2-6 nm after 2 hours [6] [12]. It can therefore be concluded that at these temperatures the precipitation of the copper particles has favorable kinetics, while the various softening mechanisms do not.

In the 520 °C to 620 °C range, the hardness of 15-5 PH will again rapidly peak, but then undergo a steady decrease as aging time increases, as shown by Peng et al [12]. Microstructural studies done at these temperatures show copper precipitates with sizes from 12 nm and up after 2 hours [6] [7] [12]. As was discussed earlier, at these temperatures the martensite matrix begins to relieve internal stresses, as dislocations begin to congregate into dislocation cells [13] [14]. A small but significant reversion to austenite is also known to happen, and all of these changes will have an effect on the hardness of 15-5 PH [13] [14].

With this discussion, the effect of the aging treatments on the AM samples that were not solution heat treated can be described. In Figure 3.1 and Table 3.2, the hardness of the samples is inversely proportional to the time and temperature at which they are heat treated. In addition, the TEM results in this study show precipitate sizes approximately 30% smaller than those found in both the solution heat treated AM samples and the traditional samples for the H1025 samples. While the initial formation of the copper precipitates cannot be remarked on, it is obvious that the growth of the precipitate particles has been retarded by some

mechanism. One potential explanation of this lower growth rate in the non-solution heat treated sample is the thermodynamic driving force of the precipitation reaction, causing a decreased growth rate. With these facts in mind, the microstructural evolution of the heat-treated samples can be hypothesized.

The reduction in hardness in these samples indicates that the hardening effect of the copper precipitation was overcome by one or a combination of the softening effects. Determination of the exact reason is difficult, but several likely reasons could be put forth. Firstly, the microstructure of the as-received AM samples in our previous study appeared to exhibit nanoscale particles that may be already existent as copper precipitates in the system. If these particles exist and are the expected copper precipitates, the as-received microstructure of the AM material already exhibited some of the hardness increase expected from the precipitation of copper particles. This would mean the microstructural evolution would involve predominantly softening effects. Another potential reason for the hardness reduction is the combined effect of the reduction of internal stress and dislocation density decrease in the martensite, which decreases hardness faster than the hardening increase imparted by the copper precipitates.

The solution heat treated microstructure can be expected to fairly closely reflect the TM samples, as hardness values for both specimen types were within standard deviation of each other for the majority of the aging heat treatments. There is one sample, H1150-M, which exhibited an increase in Vickers microhardness value of approximately 20.

The H1150-M heat treatment schedule calls for a two-step treatment, beginning with a 2-hour treatment at 760 °C followed by air cooling. After cooling, an additional 4-hour heat treatment at 621 °C is carried out. As was covered earlier, this 760 °C temperature is in range of the low end of the austenite reversion temperature. Brandl et al. [8] showed that in temperatures around 745 °C the nickel and chromium partitioning involved in the austenite reversion transformation as well as the austenite reversion itself are already occurring. It follows, therefore, that some retained feature of the specimens AM origin affects one or both of these mechanisms in some way, though what effect occurs exactly cannot be elucidated with the current dataset. It is also worth mentioning that, though the hardness of the H1150 A and C specimens are within the standard deviation of the H1150 A sample, there may be some

difference between those samples as well. If such is the case, the second step of the H1150-M treatment may also contribute to the increased hardness the H1150-M type A exhibited.

The microstructural evolution of the non-solution heat treated samples should exhibit microstructures with varying amounts of internal stress relaxation. The H900 B sample had a 2-hour heat treatment at a temperature well below the martensite tempering temperature range, but the slight reduction in hardness is most likely attributable to some softening effect in the martensite matrix. It should therefore closely resemble the as-received material and should the copper particles exist in the as-received material, this resemblance will be even closer.

It's expected that the H925 B and H1025 B samples should have microstructures that resemble each other, according to their similar hardness values. Both should exhibit microstructures primarily of martensite with relieved internal stresses compared to the as-received material and some level of dislocation arrangement, though the H1025 sample most likely has larger copper precipitates.

H1075 B and H1100 B should exhibit microstructures of similar comprability, according to the small hardness difference between the two. The copper particles in both samples can be assumed to still be of a size to be expected to exhibit coherence with the matrix in these samples. The hardening effect caused by the copper precipitates in AM materials in this temperature region appears to be comparable to the softening effect caused by the creation of dislocation cells, the reduction in internal stress in the martensitic matrix, and potential austenite reversion.

H1150 B shows an increased drop in hardness, which could be due to copper precipitates becoming large enough be increasingly incoherent with the matrix, as well as the other softening effects in the martensite matrix.

H1150-1150 B is difficult to discuss, as its hardness is very similar to that exhibited by H1150 B. It could be that the copper precipitates have reached their maximum effect, and there is no further evolution of the martensitic matrix. Further information is needed in this case.

H1150-M B shows a large drop in hardness, down to values expected from TM after a solution heat treatment. Due to the 760 °C temperature heat treatment, large amounts of

austenite reversion should occur in the sample. In addition, though no reference as to the dissolution temperature of the copper particles in 15-5 PH could be located, a reference was obtained examining the parent alloy 17-4 PH. In 17-4 PH, the dissolution temperature of copper was predicted to be 735 °C [14]. Due to the similar composition of the alloys it can be assumed that the dissolution point of copper particles in 15-5 PH is similar. Therefore, it can be speculated that in H1150-M B the matrix martensite closely resembles the TM material, and the copper particles may have grown to be incoherent with the matrix. Further examination of this microstructure is needed as well.

3.4.3 Strengthening Mechanisms in 15-5PH

There are multiple hardening mechanisms in 15-5 PH, but herein only the main mechanisms will be covered. 15-5 PH gets its hardness from its martensitic structure and its precipitated particles of copper. There are various strengthening mechanisms in martensite, though no agreement on the identity of the main strengthening mechanisms exist, the most potent mechanisms are known to be grain size strengthening and dislocation strengthening [13].

3.4.3.1 Grain Size Strengthening in Martensite

Martensitic steels are known to display a Hall-Petch relationship between their yield strength and their effective grain size [13]. There are three effective grain sizes that can be chosen, prior austenite grain size, martensite packet size, and martensite block size [13]. All of these features exhibit high angle grain boundaries, boundaries with an angle higher than 15°. While prior austenite grain size needs no further explanation, packet size and block size might. A martensite block is a group of laths with similar crystallographic orientations, with low angle boundaries between them. A martensite packet is a group of martensite blocks that have similar habit planes. A habit plane is the interface plane between austenite and martensite on a macroscopic scale. All of these sizes have been shown to be acceptable for use in determination of the grain boundary effect, as long as the appropriate constants are used.

$$\sigma_{ys} = \sigma_0 + k_y D^{-1/2} \tag{3.2}$$

Equation 3.2 is the Hall-Petch relationship expected in martensite [13]. In this equation, σ_{ys} is the yield strength of the steel, σ_o is a summation of various other strengthening mechanisms, including iron lattice friction stress, precipitation strengthening, dislocation/lath strengthening, and solid solution strengthening. In this equation, the precipitation strengthening referred to is the precipitation of iron carbides in martensite, which can be considered negligible in 15-5 PH SS due to its low carbon content. These mechanisms are not expected to be dependent on the grain size of the martensite. The term k_y is the locking parameter of the steel. This locking parameter is affected by the alloying additions in the steel and must therefore be determined for individual alloys. The final term, D is the effective grain size chosen. Unfortunately, the author was unable to locate a source for the locking parameter of 15-5 PH, preventing determination of the grain size effect without further data collection.

3.4.3.2 Dislocation Density Hardening in Martensite

The dislocation density in a martensitic structure is known to be a significant strengthening mechanism in martensite and may be the most significant of the strengthening mechanisms [13]. Dislocation strengthening in martensite typically follows a Taylor model.

$$\sigma_{ys} = \sigma_0 + \alpha \bar{M} G b \rho^{0.5} \tag{3.3}$$

Equation 3.3 is the Taylor hardening model for the strengthening effect of dislocations in martensite [13]. In the equation, σ_{ys} is again the yield strength of the steel. The σ_0 and α terms are both fitting constants not influenced by dislocation density. The Taylor factor, $\bar{M}$ is known to be 2.75 in polycrystalline BCC materials [13]. G is the shear modulus of the steel, and b is the Burgers vector of the slip direction. The term ρ is the dislocation density of the steel. Unfortunately, the dislocation density in the samples must be determined before any determination of the effect of dislocation density on the samples can be determined.

3.4.3.3 Precipitation Strengthening Effect

The precipitation strengthening mechanism is the primary strengthening mechanism in 15-5 PH. The effect the precipitated copper particles have is complex, and dependent on multiple properties of the particles.

It is important to first discuss the coherency of particles, because particle coherency determines the mechanism by which particles interact with dislocations. A particle is coherent with the matrix when there is a crystallographic relationship between the two. This means that in the boundary between the particle and the matrix, the boundary atoms form unit cells containing a mix of atoms from the particle and matrix. Particles can also be partially coherent, in this case there will be some atoms of either particle or matrix that will not occupy an intended space in the unit cell. Thusly, in the boundary space of incoherent particles, multiple crystallographic defects will occur. Incoherent particles have no such crystallographic relationship, and act as a separate phase altogether.

There are two mechanisms by which particles interact with dislocation movement. These mechanisms are particle shearing and dislocation, or Orowan, looping. Coherent particles will be sheared by dislocations moving through them, as they maintain their crystallographic relations with their surroundings. Dislocations cannot travel through incoherent particles, however, as the particles boundary atoms have no relation to the matrix atoms. This requires that defects be retained around the particle, as neither matrix nor particle atoms can occupy the space required by the dislocation as it passes, leaving a dislocation loop around the particle. Particles in 15-5 PH have less coherency with the matrix as their size increases, eventually becoming incoherent altogether. The sizes of the copper precipitates contained in the H1025 samples are all of sizes to be at least partially coherent, and therefore will be modeled as coherent particles in the forthcoming examples.

In particle shearing, there are six particle properties that effect how easily the particle can be sheared, and thusly their effect on strength. These six properties are: coherency strain, stacking fault energy, ordered structure, modulus effect, interfacial energy or morphology, and lattice friction stress. As the particles in 15-5 PH are not ordered, there is no ordered structure effect to consider. Herein, the generalities of the effects with the most expected influence will be discussed, and if possible, will be examined with what data exists for the H1025 samples tested in this study. The strengthening effect caused by incoherent particles will also be evaluated.

Firstly, though a volume fraction of the precipitate particles was not determined experimentally, an approximation can be calculated assuming all copper has precipitated. In

order to do this, the density of the Fe-Cr-Ni matrix must first be determined. This determination requires the weight percent of the matrix in the material, and the weight percent of the matrix constituents in the matrix itself. Assuming all species exist in our material at the maximum allowable weight percent, the Fe-Cr-Ni matrix is 92.48% of the total material. This value can be used alongside the total weight percent of the matrix constituents in Equation 3.4 to determine the constituents weight percent of the matrix.

$$\frac{wt\%\ of\ constituen\ \ in\ material}{wt\%\ of\ matrix} = wt\%\ of\ constituent\ in\ matrix \tag{3.4}$$

Using this equation, the matrix is 77.29 wt% Fe, 16.76 wt% Cr, and 5.95 wt% Ni. These values can be used alongside the constituent densities to determine the density of the matrix in Equation 3.5.

$$D_{matrix} = \sum wt\%_{constituent} \times D_{constituent} \tag{3.5}$$

Equation 3.5 gives the matrix a density of 7.813 g/cm^3. This density can be used to find the volume fraction of precipitated copper via Equation 3.6.

$$f_{Cu} = \frac{wt\%\ Cu/_{D_{Cu}}}{wt\%\ Cu/_{D_{Cu}} + wt\%\ matrix/_{D_{matrix}}} \tag{3.6}$$

According to Equation 3.6, the volume fraction, f, of the copper precipitates is 4.07×10^{-2} vol%. This value will be used for the volume fraction of the copper particles whenever volume fraction of particles is needed.

The coherency strain is the effect of the difference in lattice parameter between the particle and the matrix. Equation 3.7 shows the relationship between this effect and the strength of the material:

$$\Delta\sigma \approx 6G(\varepsilon_{coh})^{3/2}\sqrt{\frac{fr}{b}} \tag{3.7}$$

Where Δσ is the change in strength in the material, G is the shear modulus of the matrix, f is the volume fraction of the particles, r is the radius of the particles, b is the Burgers vector, and ε_{coh} is the coherency strain, given by Equation 3.8:

$$\varepsilon_{coh} = \frac{a_{ppt} - a_{matrix}}{a_{matrix}} \tag{3.8}$$

where *a* is the lattice constant of the material. In their examination of copper particles in an iron lattice Tang et al. [16] modeled BCC copper and showed it should have a lattice constant between 0.276-0.286 nm. The larger of these values will be used in order to model the least expected coherency effect. The shear modulus of 15-5 PH is dependent on the heat treatment it has undergone. For H1025, the shear modulus is known to be 75 GPa. In lath martensite, the Burgers vector *b* is known to be $\frac{a}{2} < 1\bar{1}1 >$ the value of which should be equal to $\frac{a}{2}\sqrt{3}$. Bajguirani [6] states in his study that the lattice constant of the martensite in 15-5 PH SS is 0.2878 nm.

Using these values in Equation 3.8, the ε_{coh} value calculates to 6.94×10^{-2}. The coherency strain can then be used in Equation 3.7 to calculate expected strength increases of 319 MPa, 249 MPa, and 304 MPa for the H1025 A, B, and C samples respectively. This indicates that coherency strain is an important effect in these particles.

The shear modulus difference between the particles has a strengthening effect due to the dislocation energy being directly related to the local shear modulus. This effect is known to follow Equation 3.9:

$$\Delta\sigma \approx \frac{\Delta G}{2\pi^2}\left[\frac{3|\Delta G|}{Gb}\right]^{1/2}\left[0.8 - 0.143\ln\left(\frac{r}{b}\right)\right]^{3/2} r^{1/2} f^{1/2} \tag{3.9}$$

where *r* is the particle radius.

It can be assumed that the BCC copper particles will exhibit the same shear modulus as FCC copper, 45 GPa. Calculating the modulus strengthening effect provides values of 178 MPa, 194 MPa, and 182 MPa for the H1025 A, B, and C samples respectively. While this strengthening effect is therefore expected to be less effective than the coherency strain effect, it should still impart a significant increase to material strength.

When a dislocation shears a particle, the particles surface area increases by one Burgers vector width. As the surface area increases, the surface energy must also increase, and this increase in surface energy can only be supplied by the external stress on the object. This is the interfacial energy or morphology effect mentioned earlier. The increase in strength caused via this effect can be determined via Equation 3.10:

$$\Delta\sigma \approx \frac{2\sqrt{6}}{\pi}\gamma_s \frac{f}{r} \tag{3.10}$$

where γ_s is the particle-matrix energy, and the other terms were previously defined. This equation is defined for spherical particles, while the copper particles in 15-5 PH do form in a spherical shape, they are known to change shape as size increases. While the results obtained from the H1025 samples show spherical particles, the particle-matrix energy was unable to be located in the literature, and this effect therefore cannot be evaluated.

The relative increases expected based on these effects may indicate that the particles of one or more of the samples are not coherent, most likely the precipitates in H1025 A and C. This can be said due to the fact that the hardness of H1025 B was experimentally determined to be 50% harder than A or C, indicating a higher strength value in B. This does not agree with the calculations, which show similar relative increases for the effects that could be calculated. The effects that could not be calculated need to be further evaluated before this statements validity can be determined.

If the particles are incoherent, the strengthening mechanism caused by the particles is dislocation or Orowan looping. This increase in strength is caused by the stress required to bow a line dislocation between two particles. This effect is modeled in Equation 3.11:

$$\Delta\sigma_p = \frac{0.8\bar{M}Gb}{L} \tag{3.11}$$

where L is the interparticle spacing, $\bar{M}$ is the Taylor factor of polycrystalline BCC material with random orientation, and the other terms have been defined previously. Equation 3.12 can be used to determine the interparticle spacing:

$$L = \frac{4(1-f)r}{3f} \tag{3.12}$$

where all of these terms have been previously defined.

Using the previously calculated volume fraction gives interparticle spacing values of 289 nm, 176 nm, and 263 nm for H1025 A, B, and C respectively. The Taylor factor of the martensite is expected to be 2.75, as the carbon content is low enough to be considered BCC. Calculation of Equation 3.11 with these values provides expected strength increases of 142 MPa, 234 MPa, and 156 MPa for H1025 A, B, and C respectively. These values reflect the

experimentally determined hardness of the samples, in that H1025 A and C are similar, while B shows a 50% increase comparatively. This may also indicate incoherence in one of more of the particles, but further examination is needed.

3.5 Conclusions

The present study examined the differences in the microstructural details of the 15-5 PH SS made via DMLS versus the details of the TM 15-5 PH SS alloy after they have undergone a heat treatment regimen. This regimen either included the industrial standard solution heat treatment used on all TM 15-5 PH steel or did not. Initial examination of the VHN of the samples showed that the addition of the solution heat treatment brought those AM samples that underwent it into rough agreement with the TM alloy after heat treatment, while the AM samples that did not undergo a solution heat treatment before aging continued to have a VHN roughly 11% higher. The solution heat treatment is thought to cause this change via the complete reversion of the AM sample to austenite, resulting in a microstructure and free energy driving forces nearly identical to the TM material. Further examination of this effect is necessary to determine the validity of this statement.

On examination of sample microstructure via TEM, the size of the copper precipitates in the solution heat treated samples were of similar size to those in the TM samples, while the particles were 50% smaller in the samples without heat treatment. No difference in dispersion of particles was noticed. Assuming full precipitation of copper, a volume fraction of precipitates was determined. The effect of the particles in the H1025 samples was then evaluated relatively, assuming both coherent and incoherent particles. For coherent particles, the coherency strain is expected to have the greatest effect. The calculated values indicate incoherent particles in one or more of the H1025 samples, but more research is needed to verify this statement. Further examination is needed to better understand the microstructure and accompanying mechanical properties of the heat-treated samples.

References

[1] D. Bourell, “Perspectives on Additive Manufacturing,” Annu. Rev. Mater. Res., vol. 46, pp. 1-18, 2016.

[2] W. Frazier, “Metal Additive Manufacturing: A Review,” Journal of Mat. Eng. And Perf., Vol 23, no. 6, pp. 1917-1928, 2014.

[3] M. Seifi, A. Salem, J. Beuth, O. Harrysson, J. J. Lewandowski, “Overview of Materials Qualification Needs for Metal Additive Manufacturing,” JOM, Vol. 68, no. 3, pp. 747-764, 2016.

[4] Y. Zhang, L. Wu, X. Guo, S. Kane, Y. Deng, Y. Jung, J. Lee, J. Zhang, “Additive Manufacturing of Metallic Materials: A Review,” Journal of Mat. Eng. and perf., vol. 27, no. 1, pp. 1-13, 2018.

[5] S. Sarkar, C. S. Kumar, A. K. Nath, “Effects of heat treatment and build orientations on the fatigue life of selective laser melted 15-5PH stainless steel,” Materials Science and Engineering: A, Vol. 755, pp 235-245, 2019.

[6] H. R. H. Bajguirani, “The effect of ageing upon the microstructure and mechanical properties of type 15-5 PH stainless steel,” Materials Science and Engineering: A, vol. 338, no. 1-2, pp. 142-159, 2002.

[7] L. Couturier, F. De Geuser, M. Descoins, A. Deschamps, “Evolution of the microstructure of a 15-5PH martensitic stainless steel during precipitation hardening heat treatment,” Materials and Design, Vol. 107, pp. 416-425, 2016.

[8] D. Brandl, M. Lukas, M. Stockinger, S. Ploberger, G. Ressel, “Evidence of austenite memory in PH 15-5 and assessment of its formation mechanism,” Materials and Design, Vol. 176, 2019.

[9] K. Ishida, “Calculation of the effect of alloying elements on the M_s temperature in steels,” Journal of Alloys and Compounds, vol. 220, issues 1-2, pp 126-131, 1995.

[10] A. Zangiabadi, “Low-Temperature Intersitial Hardening of 15-5 Precipitation Hardening Martensitic Stainless Steel,” Ph.D. dissertation, Dept. of Mater. Sci. and Eng., Case Western Reserve University, Cleveland, OH, U.S., 2017. [Online]. Available: https://etd.ohiolink.edu/!etd.send_file?accession=case1480769348244855&disposition=inline

[11] H. K. D. H. Bahdeshia, *Steels: Microstructure and Properties,* 3rd ed. Burlington, MA, U.S.: Elsevier, 2006.

[12] X. Y. Peng, X. Zhou, X. Z. Hua, Z. W. Wei, H. Y. Liu, "Effect of Aging on Hardening Behavior of 15-5 Ph Stainless Steel," Journal of Iron and Steel Research, International, vol. 22, no. 7, pp. 607-614, 2015.

[13] S. C. Kennett, "Strengthening and Toughening Mechanisms in Low-C Microalloyed Martensitic Steel as Influenced by Austenite Conditioning," Ph.D. dissertation, Dept. of Metall. and Mater. Eng., CO School of Mines, Golden, CO, U.S., 2014. [Online]. Available: https://mountainscholar.org/bitstream/handle/11124/439/Kennett_mines_0052E_10444.pdf?sequence=1&isAllowed=y

[14] R. Hamlin, "Microstructural Evolution and Mechanical Properties of Simulated Heat Affected Zones in Cast Precipitation Hardened Stainless Steels 17-4 and 13-8+Mo," Ph.D. dissertation, Dept. of Mat. Sci., Lehigh University, Bethlehem, PA, U.S., 2015. [Online]. Available: https://preserve.lehigh.edu/cgi/viewcontent.cgi?article=3625&context=etd

[15] G.E. Dieter, Mechanical Metallurgy, McGraw-Hill Publishers, SI Metric Edition, Singapore, 1988.

[16] Z. Tang, M. Hasegawa, Y. Nagai, M. Saito, "Density functional study on metastable bcc copper: Electronic structure and momentum density of positron-electron pairs," Physical Review B, vol. 65, no. 19, p. 195108, 2002.

Concluding Remarks and Future Work

The present work reported on the microstructural characteristics and mechanical properties of AM 15-5 PH SS. The study found that, as received, the microstructure of AM 15-5 PH is much finer than it's TM counterpart, though both still exhibited martensitic properties, and contained similarly sized precipitates. The microhardness of the AM steel in this condition is approximately 50% harder than its counterpart. The as received steel also exhibited improved high temperature tensile strength by 30%. In creep tests, this AM material also lasted 30% longer than TM material did.

Examination of heat treatment of the AM steel showed that the addition of an industry standard solution heat treatment of 30 minutes at 1038 °C has a significant effect on the microstructure and microhardness of the material after an aging heat treatment. AM samples that underwent the solution heat treatment exhibited microhardness values much more in line with the values displayed by TM samples. This is much different than AM samples that did not have this heat treatment done, which showed microhardness values from 10% to 30% higher than the TM material. The microstructure of the solution heat treated AM samples also showed copper precipitate sizes much more in line with those of the TM samples. This is thought to be due to full reversion of the solution heat treated AM sample to austenite, resulting in a microstructure that closely resembles the TM material.

Much work needs to be done in the future with relation to this study. The present work was undertaken with a very limited amount of material available, future work should first focus on the parameters used during the DMLS process and their effect on material properties. A focus on this will allow for the determination of whether the present manufacturing parameters are the optimal parameters for all situations, or if one or more parameters can be adjusted to improve the properties of the produced material.

The current work focused on the small scale of the microstructure of the material and did not effectively describe the bulk. Future work can be done examining the amount of martensite versus austenite in the bulk of the material, as well as examining the effect of heat treatment on this ratio. Further examination of the effect of aging heat treatments on the AM material is another area with considerable work that could be done. Microstructural examination of AM samples that have undergone other heat treatments than H1025 is an

obvious example, though there are many others. Tensile and creep analysis of heat-treated AM 15-5 PH should be carried out, to determine if the increase in high temperature properties of the material remains true in these conditions.

Outside of what properties were covered in the study, fatigue testing and impact testing of AM 15-5 PH could provide interesting results and do need to be carried out. An area of particular import for 15-5 PH is its corrosion properties, and tests need to be done to ensure AM 15-5 PH still shows the high corrosion resistance expected.

Appendix A

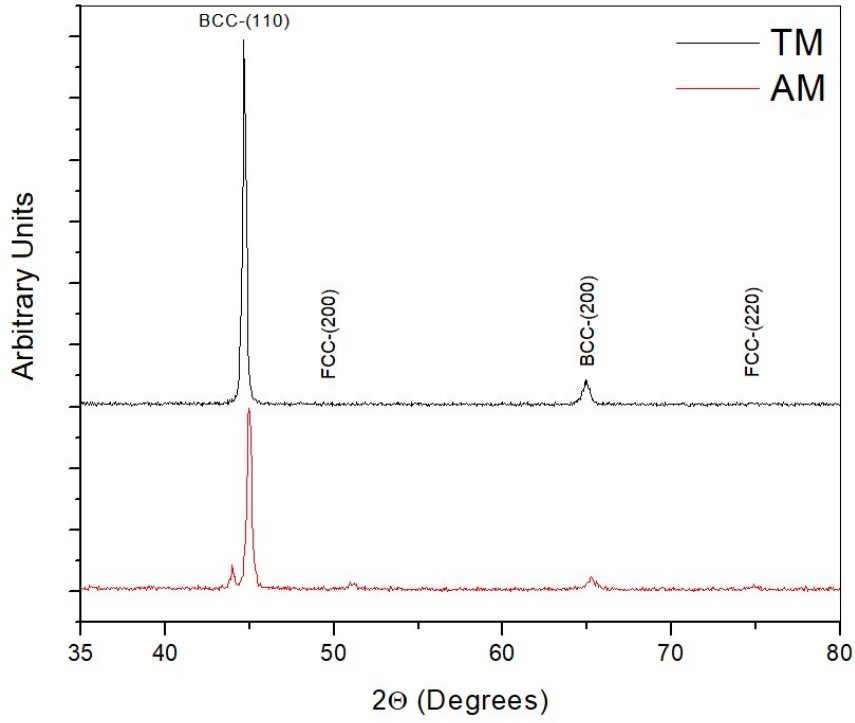

Figure A.1: XRD patterns of as-received 15-5 PH samples (both traditionally and additively manufactured). Collected in a Siemens Diffraktometer D5000, scan rate 2 hours, Cu kα wavelength source.

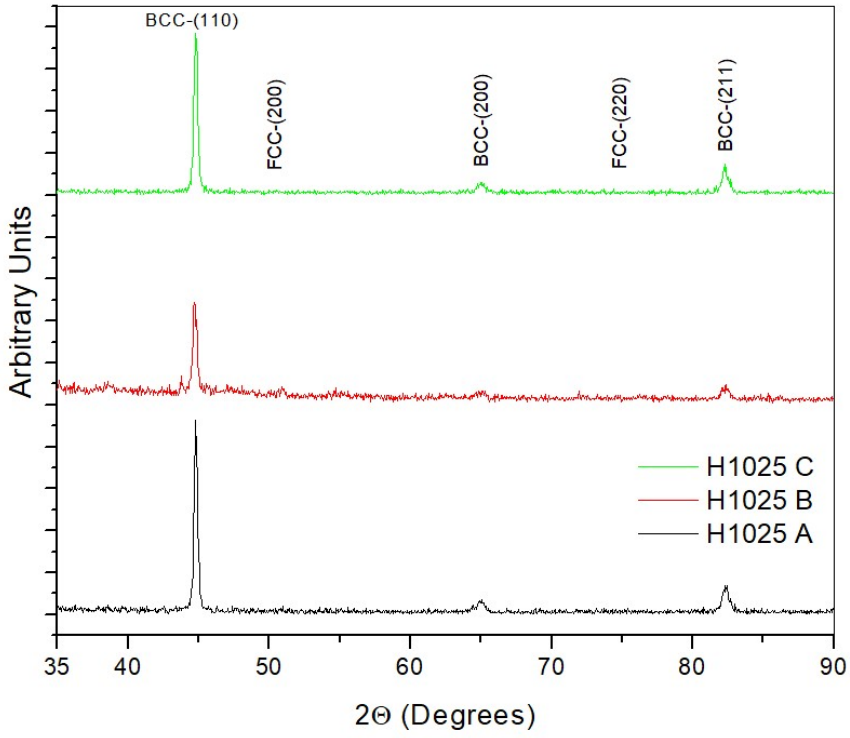

Figure A.2: XRD patterns of three different H1025 heat treated samples. Collected in a Siemens Diffraktometer D5000, scan time 2 hours, Cu kα X-ray source.